Simulating Sn Ion Collisions on $4d^n$ Targets

Laurens Johannes Kerdijk

July 31, 2020

university of groningen

Quantum Interactions and Structural Dynamics
Faculty of Science and Engineering
University of Groningen

Simulating Sn Ion Collisions on 4d^n *Targets*
Laurens Johannes Kerdijk

First examiner: prof. dr. ir. R.A. Hoekstra
Second examiner: dr. T.A. Schlathölter
Daily supervisor: K.I.J. Bijlsma, MSc

Abstract

A projectile-target collision can be described by the Binary Collision Approximation, which uses subsequent application of single binary collisions. Single elastic collisions can be depicted with Newton diagrams, in which it becomes clear that there is a maximum scattering angle, as well as two scattering energy solutions when $m_p > m_t$. From these diagrams it is also evident that only one scattering energy solution is valid when $m_p < m_t$ instead, while the recoil energy always has one solution for elastic collisions. Furthermore, SRIM and SDTrimSP were used to simulate 14 KeV ^{120}Sn ions impinging on 4d$^{\mathrm{n}}$ targets, which range from Y to Cd, with a $5°$ angle of incidence from the surface normal. Backwards sputtered particles were investigated with energy-count distributions. The results of both simulations show symmetric distributions around the surface normal of the target solid. Most sputtered particles have low energies in the range of 0 to 40 eV. SRIM shows peak and energy cutoff shifting while SDTrimSP does not. The number of counts was found to increase for heavier targets for both simulation packages. Even though the energy-count distributions from SDTrimSP are broader, SRIM generally records more sputter counts close to the xy plane for 4d$^{\mathrm{n}}$ targets.

Acknowledgements

I would really like to start by thanking everyone in the Quantum Interactions and Structural Dynamics group for the opportunity to help with research, work in this environment, and allowing me to grow as a student while having fun working on actual research. I would like to thank Ronnie Hoekstra for being a great supervisor, allowing me to work on things I am very interested in, and reassuring me when I would doubt myself. I would also like to thank Klaas Bijlsma for helping me with many general problems and scripts to process the SRIM data, as well as being very approachable. Actually, everyone seemed very approachable, which I really appreciate. I would also like to thank Sybren Koeleman for the help with setting up SDTrimSP and providing me with base processing scripts. Even though the situation we're all currently in is far from optimal, I had a truly wonderful time working with you all.

Contents

Chapter 1 Introduction

Imagine this; you have a setup with which you create a plasma using lasers to be able to generate radiation. You need a particular set of mirrors for the projection optics. Now the plasma releases certain ions which could penetrate and interact with these mirrors, possibly damaging them. Thus you would like to know how these ions interact with the material from the mirrors.

This setup is more or less reminiscent of an industrial *extreme ultraviolet* (EUV) lithography machine. In such a setup, molten Sn micro droplets are irradiated by low energy infrared pre-pulses into a flat pancake-like shape, to then be illuminated by a much more intense main pulse, which ionizes the Sn atoms and makes a dense plasma out of it [1, 2]. This sort of plasma is usually referred to as a *laser-produced plasma*, or LPP in short [1]. It is important that these ions are highly charged Sn ions in particular, since their electron configurations are emitters of the desired 13.5 nm EUV radiation when transitioning to the ground configuration [1, 2].

Collector mirrors, usually Mo–Si multi-layered mirrors capped by Ru for protective purposes, are then used to focus the EUV radiation for further lithography use [1, 3]. Mo–Si multi-layered mirrors are characterized by a 2% reflectivity band around 13.5 nm [1, 4]. Mo and Ru are $4d^n$ elements, which refers to the ground electron configuration [4]. Their ground configurations are [Kr]$4d^5 5s$ and Kr]$4d^7 5s$ respectively [4].

Now the problem is that the Sn plasma generates debris in the form of Sn ions which could have energies up to 20 KeV, and could therefore damage these mirrors [2]. Thus it is important to know how Sn ions interact with surfaces and solid targets. That is, more or less, the first goal of this thesis; simulating the interactions between 14 KeV Sn ions and $4d^n$ solid targets with a 5° angle of incidence from the surface normal, and investigating the target atoms which are removed from the material due to this interaction.

In particular, $4d^n$ refers to elements with configurations ranging from [Kr]$4d5s^2$ to [Kr]$4d^{10}5s^2$. These elements are the ones ranging from Y to Cd [4]. For this range of elements, the results obtained from simulations regarding removed particles will be compared. This might be useful in selecting potential materials as a substitute for Ru or Mo.

To be able to understand how these interactions work, it might be useful to understand just a single projectile-target collision first. There is quite a lot of theory behind these collisions, but it was not always clear how certain relations were derived and it was hard to find information on *Newton diagrams* for collisions like this, which are very useful in understanding how they work, in particular for the studied case of a heavy projectile (Sn) colliding on a lighter target atom. This leads to the second goal of the thesis; to establish a basic understanding of a single projectile-target collision and intuitively understand the dynamics of a single collision from Newton diagrams.

The last goal of the thesis is to obtain a very basic understanding on how the simulation programs used in this thesis can be operated and how the data from them can be used and processed.

Chapter 2 Projectile-Target Interaction Theory

A setup where an ion is penetrating a target can contain many interactions between different atoms within the system [5, 6]. To get a better understanding of these processes it might be best to consider only a hard-sphere collision between projectile atom with a single target atom, which can in first order model the interaction between an ion and surface atom [7]. This forms the basis of the *Binary Collision Approximation*, which treats the interaction of a projectile penetrating a solid target as a sequence of single binary collisions, making it a basis for many computer programs [5, 6]. Therefore, basic binary collision theory is treated in this chapter along with a method to find relevant energies and the construction of Newton diagrams.

2.1 ▸ Binary Collision in the Laboratory Frame

2.1.1 ▸ Conservation Laws

First of all, there are two useful frames of reference in which the ion-target collision can be treated; the frame in which the target is stationary and the center-of-mass (CoM) frame. The former will be considered as the laboratory frame, assuming the target is held stationary in the laboratory. This frame will be treated first since it provides a good introduction to the single binary collision, while the CoM frame will be discussed in section 2.2.1.

The single binary collision model is built on two fundamental laws, namely the conservation of energy and momentum. Consider a projectile of mass m_p and initial velocity $\mathbf{v}_0$. Its kinetic energy is given by $E_0 = \frac{1}{2} m_p v_0^2$ [8]. Similarly the target atom has a mass m_t , but is stationary in the laboratory frame and therefore has no kinetic energy prior to the collision. After the collision, the projectile has velocity $\mathbf{v}_p$ and has lost energy such that it has kinetic energy E_p . The target atom obtains a velocity $\mathbf{v}_t$, and thus gains kinetic energy E_t . Inelastic energy loss Q may occur in the interaction, leading to the following conservation of energy in the

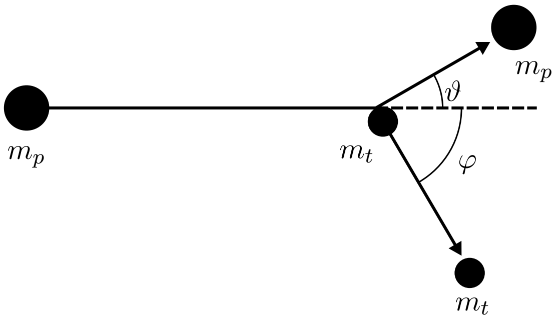

Figure 2.1: Binary collision between a projectile and a stationary target in the laboratory frame. The projectile of mass m_p scatters with a scattering angle ϑ , and the target atom of mass m_t recoils with the recoil angle φ. This figure is inspired from Eckstein [5].

laboratory frame [5];

$$\begin{aligned} E_0 &= E_p + E_t + Q\,, \\ \tfrac{1}{2}m_p v_0^2 &= \tfrac{1}{2}m_p v_p^2 + \tfrac{1}{2}m_t v_t^2 + Q\,. \end{aligned} \tag{2.1}$$

Initially, the projectile has momentum $\mathbf{p}_0$, and after the collision the projectile and target have momenta $\mathbf{p}_p$ and $\mathbf{p}_t$ respectively. Their conservation can be represented by [5];

$$\begin{aligned} \mathbf{p}_0 &= \mathbf{p}_p + \mathbf{p}_t\,, \\ m_p\mathbf{v}_0 &= m_p\mathbf{v}_p + m_t\mathbf{v}_t\,. \end{aligned} \tag{2.2}$$

Then if $v_i = |\mathbf{v}_i|$ denotes the magnitude of a particular velocity (and is thus always positive);

$$m_p v_0 = m_p v_p \cos\vartheta + m_t v_t \cos\varphi\,, \tag{2.3}$$

$$0 = m_p v_p \sin\vartheta - m_t v_t \sin\varphi\,, \tag{2.4}$$

where ϑ (theta) and φ (phi) are the projectile's *scattering angle* and the target atom's *recoil angle* respectively. Note the angles are defined such that ϑ is measured in opposite direction to φ . See figure 2.1 for a more intuitive depiction.

This description is sensible since the collision time is relatively short and The inter-atomic binding energies are much smaller than the kinetic energies [7]. The simplest case is when $Q = 0$. Then the collision is elastic such that the energy conservation is simply given by [7]

$$\begin{aligned} E_0 &= E_p + E_t\,, \\ m_p v_0^2 &= m_p v_p^2 + m_t v_t^2\,. \end{aligned} \tag{2.5}$$

2.1.2 ▶ Scattering Energy

The kinetic energy of the projectile after the interaction can be deduced from the conservation laws. In particular, the ratio between the final projectile energy E_p and the initial energy E_0 is of interest. The goal now is to express this ratio only in terms of the projectile and target masses, as well as the scattering angle, minimizing the input variables. Thus, The goal is to obtain a relation for v_p/v_0 . Equation 2.3 is a good starting point. Start by rearranging such that $\cos\vartheta$ is on one side and then square both sides [9]:

$$(m_t v_t \cos\varphi)^2 = (m_p v_0)^2 + (m_p v_p \cos\vartheta)^2 - 2m_p^2 v_0 v_p \cos\vartheta \tag{2.6}$$

Notice that $(m_p v_p \sin\vartheta)^2 = (m_t v_t \sin\varphi)^2$ from equation 2.4 can be used, along with trigonometry rules, to eliminate the dependence on φ in equation 2.6;

$$\begin{aligned}(m_t v_t \cos\varphi)^2 &= (m_t v_t)^2 \left(1 - \sin^2\varphi\right) \\ &= (m_t v_t)^2 - (m_p v_p \sin\vartheta)^2 \ .\end{aligned} \tag{2.7}$$

Therefore, equation 2.6 can be written as;

$$\begin{aligned}&(m_t v_t)^2 - (m_p v_p \sin\vartheta)^2 = (m_p v_0)^2 + (m_p v_p \cos\vartheta)^2 - 2m_p^2 v_0 v_p \cos\vartheta\,, \\ &(m_p v_p)^2 = (m_t v_t)^2 - (m_p v_0)^2 + 2m_p^2 v_0 v_p \cos\vartheta\,.\end{aligned}$$

Divide both sides by $(m_p v_0)^2$;

$$\left(\frac{v_p}{v_0}\right)^2 = \left(\frac{m_t v_t}{m_p v_0}\right)^2 - 1 + 2\frac{v_p}{v_0}\cos\vartheta\,. \tag{2.8}$$

From the conservation of energy the following relation can be obtained;

$$\begin{aligned}&m_t v_t^2 = m_p v_0^2 - m_p v_p^2 - 2Q\,, \\ &\left(\frac{m_t v_t^2}{m_p v_0^2}\right) = 1 - \left(\frac{v_p}{v_0}\right)^2 - \frac{2Q}{m_p v_0^2} \\ &\left(\frac{m_t v_t}{m_p v_0}\right)^2 = \frac{m_t}{m_p}\left[1 - \left(\frac{v_p}{v_0}\right)^2 - \frac{Q}{E_0}\right] \ .\end{aligned}$$

Substitute this into equation 2.8;

$$\begin{aligned}\left(\frac{v_p}{v_0}\right)^2 &= \frac{m_t}{m_p} - \frac{m_t v_p^2}{m_p v_0^2} - \frac{m_t Q}{m_p E_0} - 1 + 2\frac{v_p}{v_0}\cos\vartheta\,, \\ 0 &= \left(\frac{v_p}{v_0}\right)^2 \left[1 + \frac{m_t}{m_p}\right] - \left(\frac{v_p}{v_0}\right)[2\cos\vartheta] + \left[1 - \frac{m_t}{m_p} + \frac{m_t Q}{m_p E_0}\right] \ .\end{aligned}$$

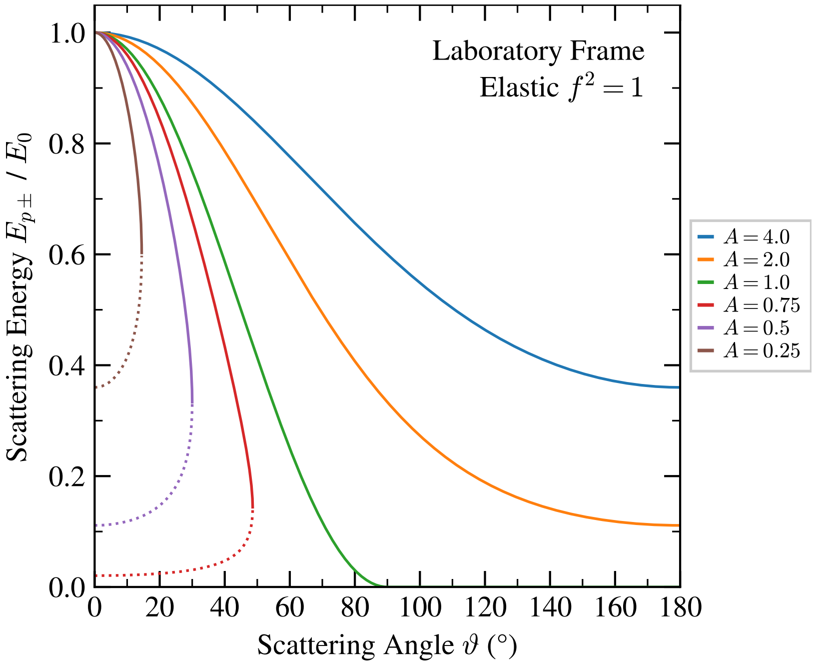

Figure 2.2: This plot shows the relation between the scattering energy $E_{p\pm}/E_0$ and the scattering angle ϑ in the laboratory frame for an elastic collision ($f^2 = 1$). The solid lines represent E_{p+} while the dotted lines represent E_{p-}. Notice that the projectile does not have any remaining energy after $\vartheta = 90°$ if $A = 1$, and that the maximum scattering angle ϑ_{max} is reached at the transition between E_{p+} and E_{p-}.

This can be solved for v_p/v_0, and thus E_p/E_0 is obtained. With $A = m_t/m_p$;

$$\frac{v_p}{v_0} = \frac{2\cos\vartheta \pm \sqrt{4\cos^2\vartheta - 4(1+A)\left(1 - A + A\frac{Q}{E_0}\right)}}{2(1+A)}$$

$$= \frac{\cos\vartheta \pm \sqrt{(1-\sin^2\vartheta) - 1 + A - A + A^2\left(1 - \frac{Q}{E_0} - \frac{Q}{E_0 A}\right)}}{1+A} .$$

Therefore, the projectile's kinetic energy in the laboratory frame, the *scattering energy*, is given by;

$$\boxed{\frac{E_{p\pm}}{E_0} = \left(\frac{\cos\vartheta \pm \sqrt{(Af)^2 - \sin^2\vartheta}}{1+A}\right)^2} , \tag{2.9}$$

where $f^2 = 1 - \frac{1+A}{A}\frac{Q}{E_0}$ [5]. Here it is assumed that the collision is instantaneous. The sign in the subscript of $E_{p\pm}$ indicates whether the plus or minus sign is referred to. This relation is in agreement with literature [5]. notice that this relation is symmetric in ϑ and the argument of the square root can become negative when $Af < 1$, introducing a *maximum scattering angle*. This maximum angle can be found from;

$$\vartheta_{\text{max}} = \pm \arcsin{(Af)} \,. \tag{2.10}$$

If $Af \geq 1$, the scattering angle is not bounded; $-180° \leq \vartheta \leq 180°$.

For an elastic collision, $f^2 = 1$, resulting in a more familiar equation [7, 9];

$$\frac{E_{p\pm}}{E_0} = \left(\frac{\cos\vartheta \pm \sqrt{(m_t/m_p)^2 - \sin^2\vartheta}}{1 + m_t/m_p} \right)^2 \,, \tag{2.11}$$

which is plotted in figure 2.2.

$E_{p\pm}$ has the two solutions but they are not always both valid. In the case where $Af < 1$, both E_{p+} and E_{p-} are, while only E_{p+} is valid if $Af \geq 1$ [5]. For an elastic collision this means that both are valid when $m_p > m_t$, while only E_{p+} is valid if $m_p \leq m_t$. This is not immediately obvious and the reason for this will be investigated in section 2.2.2.

2.1.3 ► Recoil Energy

The ratio between the kinetic energy of the recoiled target atom E_t and the initial projectile energy E_0 can be found in a very similar way. The goal is again to express this ratio only in terms of the projectile and target masses, and the recoil angle. Start again by rearranging equation 2.3 were $\cos\vartheta$ is now on one side and square both sides;

$$(m_p v_p \cos\vartheta)^2 = (m_p v_0)^2 + (m_t v_t \cos\varphi)^2 - 2 m_p m_t v_0 v_t \cos\vartheta \,. \tag{2.12}$$

Similarly to equations 2.7;

$$(m_p v_p \cos\vartheta)^2 = (m_p v_p)^2 - (m_t v_t \sin\varphi)^2 \,, \tag{2.13}$$

which results in

$$\begin{aligned} (m_p v_p)^2 - (m_t v_t \sin\varphi)^2 &= (m_p v_0)^2 + (m_t v_t \cos\varphi)^2 - 2 m_p m_t v_0 v_t \cos\varphi \,, \\ (m_t v_t)^2 &= (m_p v_p)^2 - (m_p v_0)^2 + 2 m_p m_t v_0 v_t \cos\varphi \,. \end{aligned}$$

Divide both sides by $m_t m_p v_0^2$;

$$\frac{m_t v_t^2}{m_p v_0^2} = \frac{m_p v_p^2}{m_t v_0^2} - \frac{m_p}{m_t} + 2\frac{v_t}{v_0}\cos\varphi \,. \tag{2.14}$$

Use energy conservation again to find a substitution for v_p/v_0;

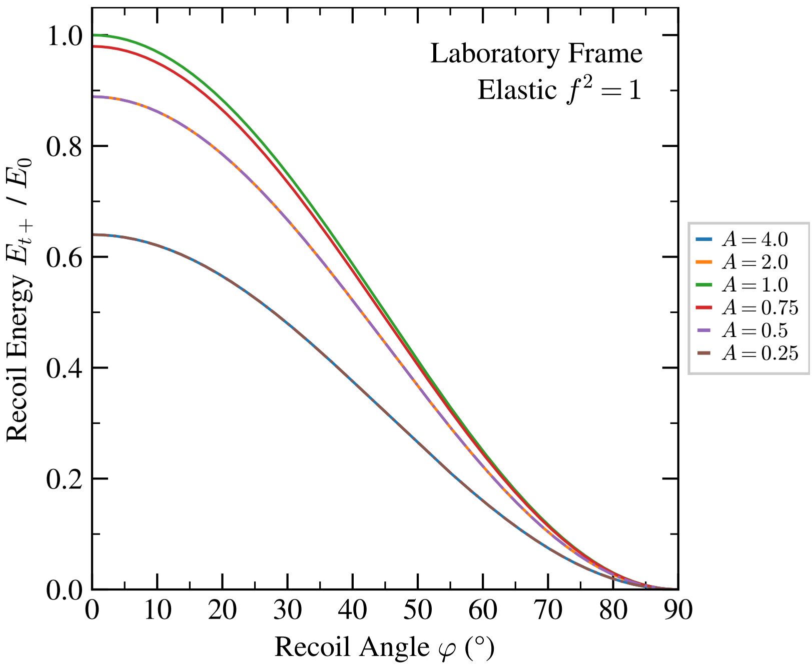

Figure 2.3: This plot shows the relation between the recoil energy E_{t+}/E_0 and the recoil angle φ in the laboratory frame for an elastic collision ($f^2 = 1$). In this case, there is no E_{t-}. Certain lines overlap. This is due to the nature of the amplitude; $4A/(1+A)^2$. In particular, $A = 2$ & $A = 0.5$ overlap, and $A = 4$ & $A = 0.25$ overlap.

$$\begin{gathered}
m_p v_p^2 = m_p v_0^2 - m_t v_t^2 - 2Q\,, \\
\frac{m_p v_p^2}{m_t v_0^2} = \frac{m_p}{m_t} - \left(\frac{v_t}{v_0}\right)^2 - \frac{m_p Q}{m_t E_0}\,.
\end{gathered}$$

Therefore, using substitution into equation 2.14;

$$\left(\frac{v_t}{v_0}\right)^2 \left[1 + \frac{m_t}{m_p}\right] - \left(\frac{v_t}{v_0}\right) [2\cos\varphi] + \left[\frac{m_p Q}{m_t E_0}\right] = 0$$

This can be solved for v_t/v_0. Recall that $A = m_t/m_p$;

$$\begin{aligned}
\frac{v_t}{v_0} &= \frac{2\cos\varphi \pm \sqrt{4\cos^2\varphi - 4\frac{1+A}{A}\frac{Q}{E_0}}}{2\,(1+A)} \\
&= \frac{\cos\varphi \pm \sqrt{1 - \frac{1+A}{A}\frac{Q}{E_0} - \sin^2\varphi}}{1+A}\,.
\end{aligned}$$

Therefore, the target atom's kinetic energy in the laboratory frame, the *recoil energy*, is given by;

$$\boxed{\frac{E_{t\pm}}{E_0} = A\left(\frac{\cos\varphi \pm \sqrt{f^2 - \sin^2\varphi}}{1+A}\right)^2}\,, \tag{2.15}$$

which is consistent with the literature [5]. Notice that E_t is symmetric in φ. For an elastic collision, $\cos\varphi \pm \sqrt{1-\sin^2\varphi} = \cos\varphi \pm \cos\varphi$, which is either 0 or $2\cos\varphi$. Therefore, the recoil energy in the laboratory frame for an elastic collision can be expressed as [2, 7];

$$\frac{E_{t+}}{E_0} = \frac{4m_t m_p}{\left(m_t + m_p\right)^2}\cos^2\varphi\,, \tag{2.16}$$

which is plotted in figure 2.3. Only one solution exists for the recoil energy when the collision is elastic, whereas the scattering energy has two solutions. Unlike ϑ, the recoil angle is bounded by $-90° \leq \varphi \leq 90°$ [7].

2.1.4 ► Angular Relationship for an Elastic Collision

Due to the conservation of energy and momentum, the scattering and recoil angles are related to each other. Since the final elastic scattering energy has two solutions, it is much more straightforward to find an equation for φ than it is for ϑ for an elastic collision. This means that φ has two solutions as well in the same region. To find these, start by considering the conservation of energy for elastic collisions in the laboratory frame as seen in equation (2.5). Since E_t depends on φ, the relation can be written as follows:

$$1 = \frac{E_{p\pm}}{E_0} + \frac{E_t}{E_0} = \frac{E_{p\pm}}{E_0} + \frac{4m_t m_p}{\left(m_t + m_p\right)^2}\cos^2\varphi\,.$$

Note that $E_{p\pm}$ depends on ϑ and not on φ; $E_{p\pm} = E_{p\pm}(\vartheta)$;

$$\begin{aligned} \cos^2\varphi &= \frac{\left(m_t + m_p\right)^2}{4m_t m_p}\left[1 - \frac{E_{p\pm}(\vartheta)}{E_0}\right], \\ \varphi_\pm &= \arccos\left(\left[m_t + m_p\right]\sqrt{\frac{1 - \left[E_{p\pm}(\vartheta)/E_0\right]}{4m_t m_p}}\right). \end{aligned} \tag{2.17}$$

This function is plotted in figure 2.4. Since φ depends on $E_{p\pm}$, it is subject to the same sign validity problem. For $m_p > m_t$, both φ_+ and φ_- are valid, while only φ_+ is valid if $m_p \leq m_t$. As mentioned, this will be discussed in section 2.2.2.

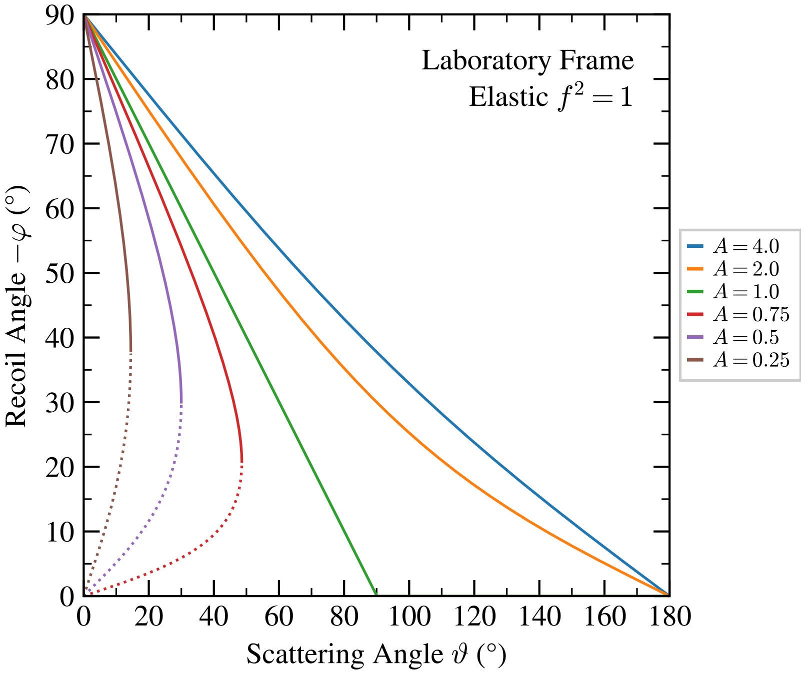

Figure 2.4: This plot shows the relation between the recoil angle $\varphi_\pm$ and the scattering angle ϑ in the laboratory frame for an elastic collision ($f^2 = 1$). Since $\varphi\pm$ depends on $E_{p\pm}(\vartheta)$, some of its characteristics, such as ϑ_{max}, are carried over.

2.2 ▸ Newton Diagrams

2.2.1 ▸ The Center-of-Mass Frame

In the previous sections a binary collision was treated in the laboratory frame. It was found that the scattering energy has two solutions; E_{p+} and E_{p-}. It was claimed, while left unexplained, that only E_{p+} is valid if $Af \geq 1$, while both are valid otherwise. To get an idea on why this is the case, it is useful to represent this collision graphically using a *Newton diagram*. Such a diagram shows the transformation of velocities from the laboratory frame to the center-of-mass frame, before and after the collision [10]. Therefore further discussion of the collision in the center-of-mass frame is necessary.

In the center-of-mass frame, the target atom is not stationary anymore. Therefore the conservation of energy takes the following form in the center-of-mass frame [5];

$$\begin{aligned} \bar{E}_p + \bar{E}_t &= \bar{E}'_p + \bar{E}'_t + Q\,, \\ \tfrac{1}{2}m_p\bar{v}_p^2 + \tfrac{1}{2}m_t\bar{v}_t^2 &= \tfrac{1}{2}m_p\bar{v}_p'^2 + \tfrac{1}{2}m_t\bar{v}_t'^2 + Q\,. \end{aligned} \tag{2.18}$$

A bar above a variable denotes it being with respect to the center-of-mass frame. The prime indicates variables after the collision.

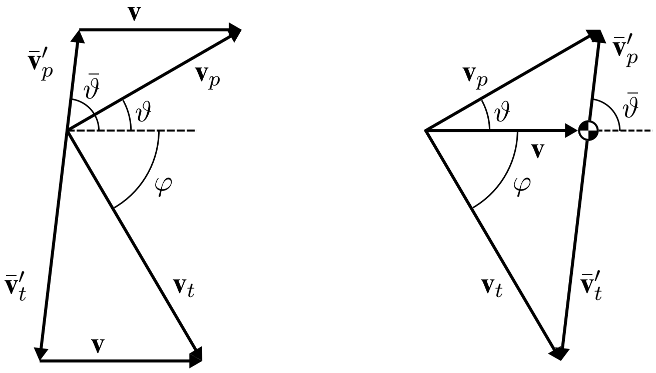

(a) **(b)**

Figure 2.5: (a): This illustration shows the relations between the velocities from both the laboratory frame and the center-of-mass frame. When changing from the laboratory frame to the CoM frame, the velocity vectors only transform in the $-\hat{\mathbf{v}}$ direction, which in this figure is horizontal. This illustration is inspired from Eckstein [5]. (b): This illustration depicts the basis for the Newton Diagram where v_p and $\bar{v}'_p$ share the same end point, and likewise for v_t and $\bar{v}'_t$.

The center-of-mass behaves as if it is a single particle [8]. Since it is at rest in the center-of-mass frame, its momentum $\bar{\mathbf{P}}$, the total momentum, equals zero in this frame [5]. Thus, the conservation of momentum takes the following form in the center-of-mass frame;

$$\begin{aligned} \bar{\mathbf{p}}_p + \bar{\mathbf{p}}_t &= \bar{\mathbf{p}}'_p + \bar{\mathbf{p}}'_t = 0\,, \\ m_p\bar{\mathbf{v}}_p + m_t\bar{\mathbf{v}}_t &= m_p\bar{\mathbf{v}}'_p + m_t\bar{\mathbf{v}}'_t = 0\,. \end{aligned} \tag{2.19}$$

Note that because of this conservation, $\bar{\mathbf{v}}'_p$ and $\bar{\mathbf{v}}'_t$ are in the same direction, but opposite to each other; $m_p\bar{\mathbf{v}}'_p = -m_t\bar{\mathbf{v}}'_t$. This results in only one scattering angle $\bar{\vartheta}$ in the center-of-mass frame, as opposed to a scattering angle and recoil angle in the laboratory frame [5]. The scattering angle $\bar{\vartheta}$ will be referred to as the *center-of-mass angle* (or CoM angle) to lift confusion.

The velocities in the laboratory frame and the center-of-mass frame are related as follows [5];

$$\begin{aligned} \bar{\mathbf{v}}_p &= \mathbf{v}_0 - \mathbf{v}\,, & \bar{\mathbf{v}}_t &= -\mathbf{v}\,, \\ \bar{\mathbf{v}}'_p &= \mathbf{v}_p - \mathbf{v}\,, & \bar{\mathbf{v}}'_t &= \mathbf{v}_t - \mathbf{v}\,, \end{aligned} \tag{2.20}$$

where $\mathbf{v}$ is the velocity of the center-of-mass in the laboratory frame. The center-of-mass always lies on the axis between the two particles in this single binary collision. Therefore, due to the target initially being at rest in the laboratory frame, the two particles' momenta do not change in the direction perpendicular to the incident trajectory $\hat{\mathbf{v}}_0$ (assumed to be straight) upon changing from the laboratory frame to the center-of-mass frame. As a result the velocities only transform in the direction of the incident trajectory; the velocities originally from the laboratory frame transform in only one direction $-\hat{\bar{\mathbf{v}}}_p = -\hat{\mathbf{v}}_0 = -\hat{\mathbf{v}}$. A depiction of this shown in figure 2.5 (a). This is even more evident when relating the velocities in both frames using the conservation of momentum and the CoM angle $\bar{\vartheta}$ discussed before [5];

$$\begin{aligned} \bar{v}_p' \sin\bar{\vartheta} &= v_p \sin\vartheta\,, & \bar{v}_p' \cos\bar{\vartheta} &= v_p \cos\vartheta - v\,, \\ \bar{v}_t' \sin\bar{\vartheta} &= v_t \sin\varphi\,, & -\,\bar{v}_t' \cos\bar{\vartheta} &= v_t \cos\varphi - v\,. \end{aligned} \tag{2.21}$$

Therefore, a diagram can be constructed were the origins of the velocity vectors of each frame are separated by v such that v_p and $\bar{v}_p'$ share the same end point, and likewise for v_t and $\bar{v}_t'$. This is the basis for the Newton diagram, depicted in figure 2.5 (b). In this basic illustration it is shown how the velocities on both frames relate to each other. The angle between v_p and v is the scattering angle ϑ, while the angle between v_t and v is the recoil angle φ. In the case of elastic scattering, more interesting properties can be illustrated using a more sophisticated Newton diagram.

2.2.2 ▶ Diagrams for Elastic Collisions

For an elastic collision, $Q = 0$ in equation 2.18;

$$\begin{aligned} &\bar{E}_p + \bar{E}_t = \bar{E}_p' + \bar{E}_t'\,, \\ &m_p\bar{v}_p^2 + m_t\bar{v}_t^2 = m_p\bar{v}_p'^2 + m_t\bar{v}_t'^2\,. \end{aligned} \tag{2.22}$$

From the conservation of momentum, illustrated in equation 2.19, it can be shown that;

$$\bar{v}_t = \frac{m_p}{m_t}\bar{v}_p \tag{2.23}$$

Therefore, the following can be deduced using the relations above;

$$\begin{gathered} m_p\bar{v}_p^2 + \frac{m_p^2}{m_t}\bar{v}_p^2 = m_p\bar{v}_p'^2 + \frac{m_p^2}{m_t}\bar{v}_p'^2\,, \\ \bar{v}_p^2\left(m_p + \frac{m_p^2}{m_t}\right) = \bar{v}_p'^2\left(m_p + \frac{m_p^2}{m_t}\right)\,, \\ \boxed{\bar{v}_p = \bar{v}_p'}\,. \qquad \text{Similarly,} \quad \boxed{\bar{v}_t = \bar{v}_t'}\,. \end{gathered}$$

This is a remarkable result! Regardless of their direction, the magnitudes of the velocities before and after the collision are the same for each particle and for elastic scattering in the center-of-mass frame! Therefore, two circles of radius $\bar{v}_p = \bar{v}_p'$ (the *projectile circle*) and $\bar{v}_t = \bar{v}_t'$ (the *target circle*) can be drawn around the center-of-mass respectively. The velocity vectors $\bar{\mathbf{v}}_p'$ and $\bar{\mathbf{v}}_t'$ can point to any point on their respective circle, as long as $\bar{\mathbf{v}}_p' \propto -\bar{\mathbf{v}}_t'$. Since $\bar{\mathbf{v}}_t = -\mathbf{v}$, the 'origin point'

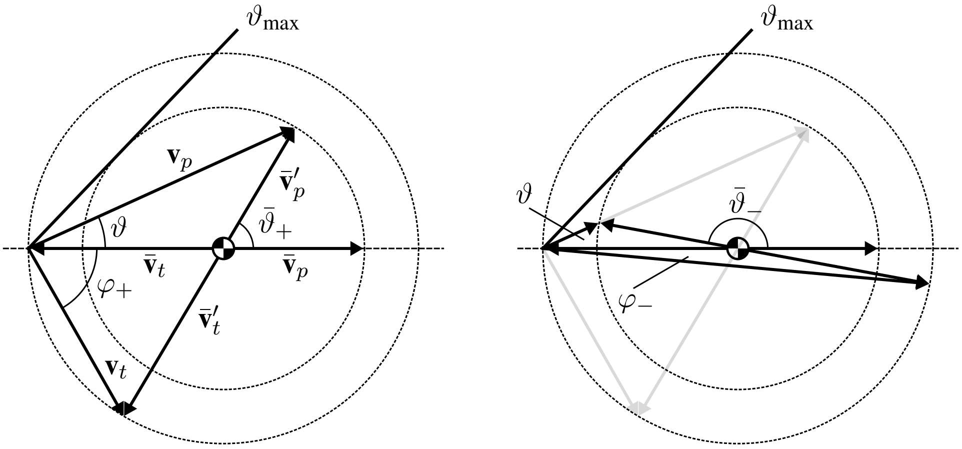

Figure 2.6: Case 1; $\boldsymbol{m_p > m_t}$. These two diagrams can intuitively show why two scattering energy solutions $E_{p\pm}$ are valid for the same scattering angle ϑ. These diagrams portray elastic collisions. The left diagram shows the positive sign being used while the right diagram shows how the negative sign compares with the positive sign. These diagrams also show how the maximum scattering angle ϑ_{max} comes into play.

for the laboratory frame vectors lies on the target circle (see equation 2.20). Notice that the recoil angle is always bounded by $-90° \leq \varphi \leq 90°$.

Now this is where two separate cases can be distinguished, namely the cases $m_p > m_t$ and $m_p \leq m_t$. In the former case, of which the diagrams are shown in figure 2.6, it can be observed that $\bar{v}_p' < \bar{v}_t'$, due to equation 2.23. Therefore the target circle is larger than the projectile circle such that the laboratory frame origin point lies outside the projectile circle. Now the following observation can be made; While $-180° \leq \bar{\vartheta} \leq 180°$, $-\vartheta_{\text{max}} \leq \vartheta \leq \vartheta_{\text{max}}$. The scattering angle is bounded by ϑ_{max}, since the velocity vector $\mathbf{v}_p$ can not make a larger angle with $-\bar{\mathbf{v}}_t$, as it has to have its endpoint on the projectile circle. This phenomenon was observed before and described with equation 2.10.

It can also be observed that one particular scattering angle can correspond to two different recoil angles, precisely because the target circle is larger. Moreover, this means one scattering angle can correspond to two different velocity magnitudes v_p, resulting in two different kinetic energies for the projectile after the collision in the laboratory frame. This was also observed before in equation 2.9, since it has two separate solutions; E_{p+} and E_{p-}.

In the case where $m_p \leq m_t$, which is depicted in figure 2.7, the scattering angle is not bounded, therefore $-180° \leq \vartheta \leq 180°$. Moreover, it can be observed that one particular scattering angle does not correspond to two recoil angles anymore, and thus only one kinetic energy for the projectile after the collision is possible in the laboratory frame. The valid solution from equation 2.9 can be found by finding a relation between the CoM angle $\bar{\vartheta}$ and the scattering angle ϑ.

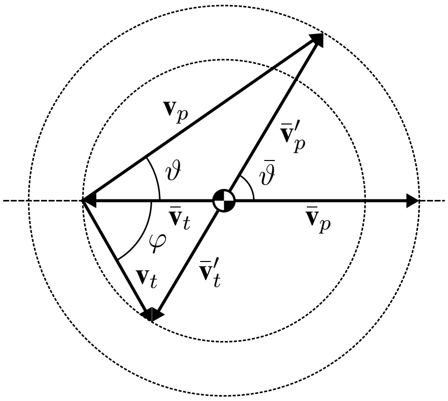

Figure 2.7: Case 2; $\boldsymbol{m_p \leq m_t}$. This figure shows that in this case, there is only one scattering energy solution E_p, along with the absence of a maximum scattering angle ϑ_{max}. This diagram portrays an elastic collision.

Let's consider an inelastic collision for the most general approach just for the moment. First, note that since $m_p \bar{v}_p \hat{\bar{\mathbf{v}}}_p = -m_t \bar{v}_t \hat{\bar{\mathbf{v}}}_t = m_t \bar{v}_t(-\hat{\bar{\mathbf{v}}}_t) = m_t \bar{v}_t \hat{\bar{\mathbf{v}}}_p$ from equation 2.19, $\bar{v}_p = A\bar{v}_t$. It is also evident that $v_0 = \bar{v}_p + v$ and $\bar{v}_t = v$ from equation 2.20 (recall that $v_i = |\mathbf{v}_i|$). This then results in the following;

$$v_0 = \bar{v}_p + v = \bar{v}_p + \bar{v}_t = \bar{v}_p + \tfrac{1}{A}\bar{v}_p \, .$$

Therefore;

$$v_0 = \left(\frac{1}{A} + 1\right) \bar{v}_p \, , \tag{2.24}$$

and similarly;

$$v_0 = (A+1)\, \bar{v}_t = (A+1)\, v \, , \tag{2.25}$$

for this system, which is in agreement with literature [5]. Then rearranging equation 2.18 and dividing both sides by $m_p \bar{v}_p^2$;

$$\begin{aligned} m_p \bar{v}_p'^2 &= m_t \bar{v}_t^2 + m_p \bar{v}_p^2 - m_t \bar{v}_t'^2 - 2Q \, , \\ \frac{\bar{v}_p'^2}{\bar{v}_p^2} &= A\frac{\bar{v}_t^2}{\bar{v}_p^2} + 1 - A\frac{\bar{v}_t'^2}{\bar{v}_p^2} - \frac{2Q}{m_p \bar{v}_p^2} \\ &= \frac{1}{A} + 1 - \frac{1}{A}\frac{\bar{v}_p'^2}{\bar{v}_p^2} - \left(\frac{A+1}{A}\right)^2 \frac{Q}{E_0} \, , \end{aligned}$$

where equation 2.24 was used for the last term to obtain E_0, along with $\bar{v}_p = A\bar{v}_t$

and $\bar{v}_p' = A\bar{v}_t'$ for the other terms. Continue rearranging;

$$\begin{aligned}
\frac{\bar{v}_p'^2}{\bar{v}_p^2}\left(1+\tfrac{1}{A}\right) &= \left(1+\tfrac{1}{A}\right) - \left(\frac{1+\frac{1}{A}}{1}\right)^2 \frac{Q}{E_0}\,,\\
\frac{\bar{v}_p'^2}{\bar{v}_p^2} &= 1 - \frac{A+1}{A}\frac{Q}{E_0} = f^2\,.
\end{aligned}$$

Therefore, using equation 2.24 and 2.25[5];

$$\frac{v_0}{\bar{v}_p'} = \frac{1+A}{Af}\,, \qquad \frac{v}{\bar{v}_p'} = \frac{1}{Af}\,. \tag{2.26}$$

This can then be used to obtain $\sin\bar{\vartheta}$ with respect to ϑ, along with equations 2.9 and 2.21;

$$\begin{aligned}
\sin\bar{\vartheta} &= \frac{v_p}{\bar{v}_p'}\sin\vartheta\\
&= \frac{v_0}{\bar{v}_p'}\sin\vartheta\left(\frac{\cos\vartheta \pm \sqrt{(Af)^2 - \sin^2\vartheta}}{1+A}\right)\\
&= \frac{1}{Af}\sin\vartheta\left(\cos\vartheta \pm \sqrt{(Af)^2 - \sin^2\vartheta}\right)\,, \qquad (2.27)
\end{aligned}$$

which is in agreement with literature [5]. For an elastic collision ($f = 1$), this means that

$$\boxed{\sin\bar{\vartheta} = \frac{1}{A}\sin\vartheta\left(\cos\vartheta \pm \sqrt{A^2 - \sin^2\vartheta}\right)}\,. \tag{2.28}$$

Only the case with the plus sign is valid if $m_p < m_t$. If the minus sign is used, a positive scattering angle between 0 and 180° would correspond to a negative $\sin\bar{\vartheta}$. However, it was established that $\bar{v}_p'\sin\bar{\vartheta} = v_p\sin\vartheta$; if ϑ is positive, $\sin\bar{\vartheta}$ should be positive as well. This problem does not occur when the positive sign is used. If $A = 1$, invalid values are obtained as well when the minus sign is used. Therefore, if $m_p \leq m_t$, only E_{p+} is valid. For extra detail, see Eckstein [5], where it was mentioned that only the positive sign is valid if $Af \geq 1$ for inelastic scattering in equation 2.27.

2.2.3 ▸ Scattering Energy With Respect to the CoM Angle

Equations 2.9 and 2.15 show the relations between the scattering energy, the recoil energy and their corresponding angles respectively in the laboratory frame. The scattering and recoil energies can also be expressed with respect to the center-of-mass angle. Firstly the scattering energy in the center-of-mass frame will be treated. To be able to do this it is useful to find relations between the center-of-mass angle and the scattering angle. From inspecting figure 2.5 and using equations 2.21 and 2.26, it can be found that [5];

$$\tan\vartheta = \frac{v_p \sin\vartheta}{v_p \cos\vartheta} = \frac{\bar{v}_p' \sin\bar{\vartheta}}{v + \bar{v}_p' \cos\bar{\vartheta}} = \frac{(\bar{v}_p'/v)\sin\bar{\vartheta}}{1 + (\bar{v}_p'/v)\cos\bar{\vartheta}} = \frac{Af\sin\bar{\vartheta}}{1 + Af\cos\bar{\vartheta}}\,,$$

which means that;

$$\begin{aligned}\sin^2\vartheta &= \frac{\left(Af\sin\bar{\vartheta}\right)^2}{\left(1 + Af\sin\bar{\vartheta}\right)^2}\cos^2\vartheta \\ &= \frac{\left(Af\sin\bar{\vartheta}\right)^2}{1 + \left(Af\cos\bar{\vartheta}\right)^2 + 2Af\cos\bar{\vartheta}}\left(1 - \sin^2\vartheta\right) \\ &= U^2\left(1 - \sin^2\vartheta\right)\,,\end{aligned}$$

where $U^2 = \left(Af\sin\bar{\vartheta}\right)^2 / \left(1 + \left(Af\cos\bar{\vartheta}\right)^2 + 2Af\cos\bar{\vartheta}\right)$ for simplicity. Then;

$$\begin{aligned}\sin^2\vartheta\left(1 + U^2\right) &= U^2\,, \\ \frac{1}{\sin^2\vartheta} &= \frac{1}{U^2} + 1\,.\end{aligned} \tag{2.29}$$

Now using equation 2.21 and 2.26, the scattering energy with respect to the center-of-mass angle can be found;

$$\frac{v_p^2}{\bar{v}_p'^2} = \frac{\sin^2\bar{\vartheta}}{\sin^2\vartheta}\,.$$

The left hand side of the equation can be worked out as follows;

$$\frac{v_p^2}{\bar{v}_p'^2} = \frac{v_0^2}{\bar{v}_p'^2}\frac{E_p}{E_0} = \left(\frac{1+A}{Af}\right)^2\frac{E_p}{E_0}\,,$$

while for the right hand side;

$$\frac{\sin^2\bar{\vartheta}}{\sin^2\vartheta} = \left(\frac{1}{U^2} + 1\right)\sin^2\bar{\vartheta}\,.$$

Therefore;

$$\begin{aligned}\frac{E_p}{E_0} &= \frac{\left(Af\sin\bar{\vartheta}\right)^2}{(1+A)^2}\left(\frac{1}{U^2} + 1\right) \\ &= \frac{\left(Af\sin\bar{\vartheta}\right)^2}{(1+A)^2}\left(\frac{1 + \left(Af\cos\bar{\vartheta}\right)^2 + 2Af\cos\bar{\vartheta}}{\left(Af\sin\bar{\vartheta}\right)^2} + 1\right) \\ &= \frac{1}{(1+A)^2}\left(1 + \left(Af\sin\bar{\vartheta}\right)^2 + \left(Af\cos\bar{\vartheta}\right)^2 + 2Af\cos\bar{\vartheta}\right) \\ &= \frac{1}{(1+A)^2}\left(1 + (Af)^2 + 2Af\cos\bar{\vartheta}\right)\,,\end{aligned}$$

which is similar to equation 2.61 in Noordam [3]. As a result, using that $\cos\bar{\vartheta} = 1 - 2\sin^2\bar{\vartheta}$, the scattering energy with respect to the center-of-mass angle is given by;

$$\boxed{\frac{E_p}{E_0} = \frac{1}{(1+A)^2}\left((1+Af)^2 - 4Af\sin^2\frac{\bar{\vartheta}}{2}\right)}\,, \tag{2.30}$$

which is in agreement with literature [5]. In this case there is no ± sign, so the energy is simply written as E_p. Note that this is still the scattering energy in the laboratory frame due to the nature of the derivation. It is just expressed with respect to the center-of-mass angle.

2.2.4 ▸ Recoil Energy With Respect to the CoM Angle

A similar approach as the one described in section 2.2.3 can be used to find the recoil energy with respect to the CoM angle. Start by finding $\tan\varphi$;

$$\tan\varphi = \frac{v_t\sin\varphi}{v_t\cos\varphi} = \frac{\bar{v}_t'\sin\bar{\vartheta}}{v - \bar{v}_t'\cos\bar{\theta}} = \frac{(\bar{v}_t'/v)\sin\bar{\vartheta}}{1 + (\bar{v}_t'/v)\cos\bar{\vartheta}}\,. \tag{2.31}$$

$(\bar{v}_t'/v)$ is not known yet however. It can be found in a similar manner to how $(\bar{v}_p'/v)$ was found though. Start by rearranging equation 2.18 and dividing both sides by $m_t\bar{v}_t^2$;

$$\frac{\bar{v}_t'^2}{\bar{v}_t^2} = A + 1 - A\frac{\bar{v}_t'^2}{\bar{v}_t^2} - \frac{1}{A}\frac{Q}{E_0}$$

where equation 2.25 was used as well as $\bar{v}_p = A\bar{v}_t$ and $\bar{v}_p' = A\bar{v}_t'$. Using a similar method as before;

$$\begin{gathered}\frac{\bar{v}_t'^2}{\bar{v}_t^2}(1+A) = (1+A)\left(1 - \frac{A+1}{A}\frac{Q}{E_0}\right)\,,\\ \frac{\bar{v}_t'^2}{\bar{v}_t^2} = f^2\,.\end{gathered}$$

Therefore, using equation 2.25 [5];

$$\frac{v_0}{\bar{v}_t'} = \frac{A+1}{f}\,, \qquad \frac{v}{\bar{v}_t'} = \frac{1}{f}. \tag{2.32}$$

These relations, as well as equation 2.21, can then be used to find $\tan\varphi$, similarly to before [5];

$$\tan\varphi = \frac{f\sin\bar{\vartheta}}{1 - f\cos\bar{\vartheta}}\,,$$

Which can be used to find $1/\sin^2\varphi$ similarly to equation 2.29;

$$\frac{1}{\sin^2\varphi} = \frac{1}{W^2} + 1 \qquad ; W^2 = \frac{\left(f\sin\bar{\vartheta}\right)^2}{1 + \left(f\cos\bar{\vartheta}\right)^2 - 2f\cos\bar{\vartheta}} \,.$$

This can then be used along with equations 2.21 and 2.32 to find E_t/E_0 with respect to the center-of-mass angle;

$$\frac{v_t^2}{\bar{v}_t'^2} = \frac{\sin^2\bar{\theta}}{\sin^2\varphi} \,,$$

of which the left hand side is equal to;

$$\frac{v_t^2}{\bar{v}_t'^2} = \frac{v_0^2}{\bar{v}_t'^2}\frac{E_t}{AE_0} = \frac{(1+A)^2}{Af^2}\frac{E_t}{E_0} \,,$$

while for the right hand side;

$$\frac{\sin^2\bar{\vartheta}}{\sin^2\varphi} = \left(\frac{1}{W^2} + 1\right)\sin^2\bar{\vartheta} \,.$$

Therefore, when supstituting W^2 ;

$$\begin{aligned} \frac{E_t}{E_0} &= \frac{A\left(f\sin\bar{\vartheta}\right)^2}{(1+A)^2}\left(\frac{1 + \left(f\cos\bar{\vartheta}\right)^2 - 2f\cos\bar{\vartheta}}{\left(f\cos\bar{\vartheta}\right)^2} + 1\right) \\ &= \frac{A}{(1+A)^2}\left(1 + f^2 - 2f\cos\bar{\vartheta}\right) \,, \end{aligned}$$

which is similar to equation 2.62 in Noordam [3]. And thus, at last, the recoil energy with respect to the center-of-mass angle is given by;

$$\boxed{\frac{E_t}{E_0} = \frac{A}{(1+A)^2}\left((1-f)^2 + 4f\sin^2\frac{\bar{\vartheta}}{2}\right)} \,, \tag{2.33}$$

which is in agreement with literature [5]. This is as far as the binary collision will be treated here in its most basic form. For further treatment on interaction potentials, cross-sections and the impact parameter, please refer to Eckstein [5].

Chapter 3 Simulating Ion-Solid Interactions

In the previous chapter, a single hard-sphere collision between two atoms was treated with a basic single binary collision. This provides a basis for understanding the interaction of ions with a solid target as a whole. In this chapter, the setup of the ion-solid interactions is treated, namely the relevant interaction types as well as the setup geometry. Moreover, two simulation packages are discussed, namely the SRIM and SDTrimSP packages.

3.1 ▸ Ion-Solid Collisions

3.1.1 ▸ Setup Geometry

In this setup, an ion beam is directed towards a solid target. The ions will interact with the atoms in the target material, after which certain particles can leave the target. It is those particles leaving the target which are of interest. To be able to characterize or categorize those particles, it is useful to discuss the setup geometry used in this thesis and simulation programs, as well as the particle trajectories.

The coordinate system is depicted in figure 3.1 and laid out as follows; $\hat{\mathbf{x}}$ is perpendicular to the target surface and is directed into the target. $\hat{\mathbf{y}}$ and $\hat{\mathbf{z}}$ are parallel to the target surface. $\hat{\mathbf{y}}$ is chosen such that the trajectory of the incident ion beam lies within the plane spanned by $\hat{\mathbf{x}}$ and $\hat{\mathbf{y}}$ (the xy plane). Many angles can be defined in such a setup. Different computer programs use different angles as well to categorize certain particles. Therefore, the following angles will be used throughout the analysis;

- ψ: Angle between the beam and the target surface.
- $\tilde{\psi}$: Angle between the incident beam and the surface normal; the *angle of incidence*.
- α: Angle between $\hat{\mathbf{x}}$ and the trajectory of the outgoing particle.
- β: Angle between $\hat{\mathbf{y}}$ and the trajectory of the outgoing particle.
- γ: Angle between $\hat{\mathbf{z}}$ and the trajectory of the outgoing particle.
- θ: Angle between the extension of the incident trajectory and the trajectory of the outgoing particles. Here it will be referred to as *escape angle*.

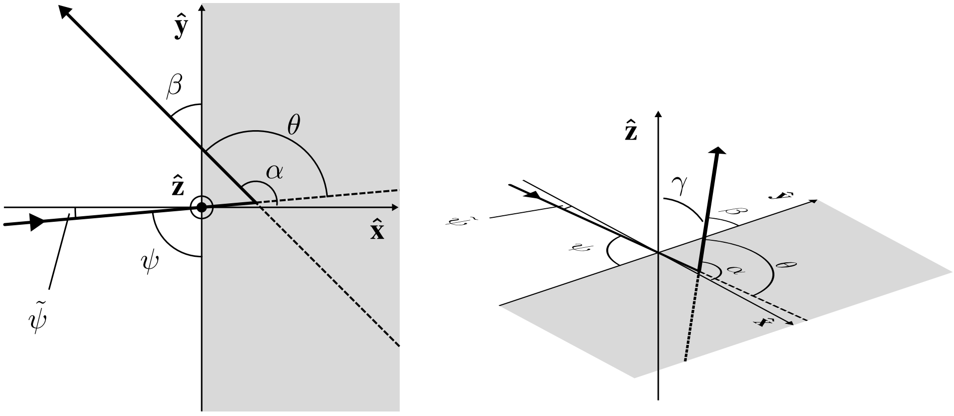

Figure 3.1: This is the coordinate system used in the thesis. The trajectory of the projectile lies within the xy plane. The trajectory of the scattered or recoiled particle can in principle be directed anywhere in 3D space and can be described by the angles α, β and γ. If this particle is escaping the target, then $90° < \alpha < 270°$ as can be observed from the diagram.

The escape angle θ is very similar to the scattering angle ϑ and recoil angle φ, but note that they are not the same. If a single scattering event occurred, then it would be equivalent depending on whether the outgoing particle is the target or the projectile. However, many outgoing particles can be a result of many interactions and collisions instead [5, 11]. Perhaps it is better not to try to relate these angles to each other too much, but rather to view θ as the angle at which a detector would be placed to investigate outgoing particles at that certain angle.

3.1.2 ▸ Interaction Types

When the incident projectile ion starts to interact with the surface, various things can happen. If the projectiles enters the target, it is scattered within the solid due to collisions of elastic energy loss with the target, while inelastic energy loss is suffered due to the interactions with electrons [5]. One option is that the projectiles lose their energy and are implanted within the solid at some point [2, 5, 6]. If the target is thin enough, the projectiles may get *transmitted* [5].

If the scattering is strong enough, the projectiles may get *backscattered*, which means that they leave the target [2]. This can be after either a single collision, or after many collisions [2, 5]. The former case is usually referred to as a *single-scattering* event, and is depicted in figure 3.2 (a) [2]. In this case, the energy of the scattered projectile would be within a band of the scattering energy shown in equation 2.9 [5]. *Quasi-single scattering*, shown in figure 3.2 (b), is when the projectile has multiple collisions with a small scattering angle, and one collision with a large scattering angle [2]. Various combinations of angles are possible which could lead to the same final angle θ, with respect to the incident trajectory, with which the projectile

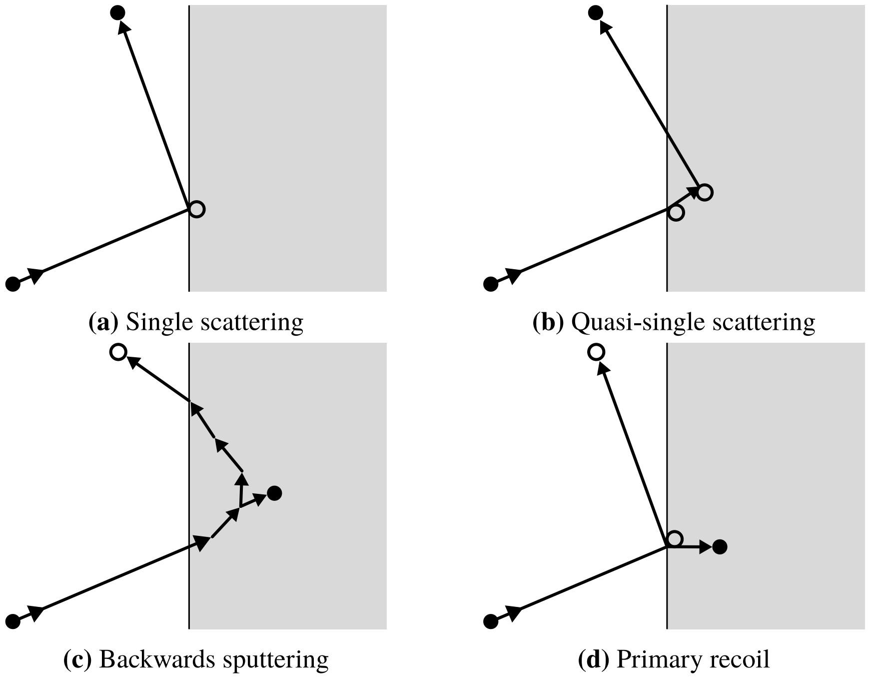
(a) Single scattering **(b)** Quasi-single scattering **(c)** Backwards sputtering **(d)** Primary recoil

Figure 3.2: This figure shows certain types of interactions and outgoing particles. The solid circles represent projectiles while the hollow circles represent target atoms [2]. Sometimes the projectile atom can be implanted within the target solid, which is shown in (c) and (d).

leaves the target. This leads to a broad energy-count distribution [2].

The penetrating projectile can cause a *cascade* within the solid target. A cascade is when the recoiled target atom collides with other target atoms, leading to more recoiled target atoms colliding with other target atoms [5]. If the kinetic energy the target atoms obtain is large enough, they could escape the solid. This is referred to as *sputtering* [5]. Sputtering specifically refers to target atoms being removed from the solid target by means of projectile bombardment [11]. If the sputtered particle leaves the target at the same surface the projectile penetrated the target, it is referred to as *backwards sputtering*[5]. This is depicted in figure 3.2 (c). Target atoms which are sputtered from the surface due to a single collision are referred to as *primary recoils*, which are illustrated in figure 3.2 (d) [2].

The elastic energy losses are gained as kinetic energy by the recoiled target atoms [5]. If a cascade is induced, this energy is distributed over many target atoms. Therefore the sputtered atoms would typically have less kinetic energy than backscattered particles would have [2]. If it is a primary recoil, it could have a kinetic energy closer to the kinetic energy of a backscattered particle [2]. The mass and energy of the projectile ions, as well as the structure and composition of the target solid would determine the number of sputtered surface particles, as well as the cascade size and penetration depth [11].

3.2 ▸ SRIM: The Stopping and Range of Ions in Matter

3.2.1 ▸ Introduction to SRIM and TRIM

The Stopping and Range of Ions in Matter, or *SRIM*, is a computer package with which ion stopping can be simulated [2]. Although it was developed to calculate stopping power tables, *Monte Carlo* simulations were included with the addition of the *TRIM* program, or the Transport of Ions in Matter, in SRIM [2, 12, 13]. A Monte Carlo simulation is one where random events are generated to be able to draw conclusions statistically [14]. TRIM in particular calculates the interactions of ions with a target which is *amorphous* [13]. Amorphous means that the material has a non-crystalline structure [15]. TRIM can simulate backscattered, sputtered and transmitted particles from a target with a composition of isotope as required by the user, and can be used to obtain statistical insight on the distribution of the energy of these particles for different escape angles θ [2].

SRIM makes use of the Ziegler-Biersack-Littmark (ZBL) universal interaction potential and Biersack's magic formula [16, 17]. SRIM can use seven different types of collision methods;

- Ion Distribution and Quick Calculation of Damage,
- Detailed Calculation with Full Damage Cascades,
- Monolayer Collision Steps / Surface Sputtering,
- Neutron / Electron / Photon Cascades,
- Various Ion Energy / Angle / Positions,

for which the details can be found in Ziegler, Biersack, and Ziegler [13]. It is suggested that the monolayer Collision Steps / Surface Sputtering method is useful for sputtering [13]. With this method the collisions will not be approximated such that every collision is evaluated in detail, and it sets the requirement that there is an ion collision in every monolayer of the target, such that the free flight path will be omitted [13, 18]. This calculation method therefore eliminates the artifacts which may be obtained due to the use of the free flight path [18]. However, the computation time when using this method is much longer [13].

With SRIM it is possible to set a variety of input parameters for the simulation. One such parameter is the angle of incidence $\tilde{\psi}$ of the ion beam. For example, if $\psi = 85°$ is desired, the angle of incidence $\tilde{\psi} = 5°$ should be used as input parameter in SRIM [13]. Along with $\tilde{\psi}$, other beam properties can be specified such as the element, its mass and its energy. It does not allow for a beam composition however, which in most cases might not be of interest to begin with. The user would be stuck with a single isotope for the ion projectiles although a more general approach can be taken by using the standard atomic weight of the element if required by the user.

The target can be specified in the form of layers in which the composition can be specified and made up of different isotopes. Manual weights and stoichiometry can be added to each isotope. The width and density of each layer can also be specified among a few other input parameters. Finally simulation specific parameters can be specified such as the number of ions which will be used in the simulation and a random number seed which can be used to make each simulation unique. If the same seed is used, the outcome of the simulation will be about the same.

3.2.2 ▸ The Output of SRIM

When an SRIM simulation is performed for backscattered and sputtered particles, the results are stored in the output files *BACKSCAT.TXT* and *SPUTTER.txt* respectively. The information about the variables stored in this file can be found within the output files, within the SRIM program or in Ziegler, Biersack, and Ziegler [19]. To be able to generate the energy-count distribution for different escape angles θ, the angles in the output of SRIM have to be interpreted.

The output files contain the energy of the outgoing particles, their positions and the direction in which they left the target. The direction is described by $\cos X$, $\cos Y$ and $\cos Z$, which seems rather counter-intuitive; how would the cosines of values on the coordinate axis describe the trajectory of the escaped particle? However, these parameters do not represent what these cosines suggest. In fact what is meant with these parameters are $\cos\alpha$, $\cos\beta$ and $\cos\gamma$ respectively [2]. Since the cosines of the angles are given, two different angles are possible for each listed output value;

$$\cos\alpha = \cos(-\alpha)\,,$$

and similarly for β and γ. Therefore, all three output values must be correctly used in order to describe the trajectory of the backscattered or sputtered particle. It can be observed that $\cos\alpha$ will always be negative for backscattered and sputtered particles though since $|\alpha| > 90°$ for these particles. Recall that x measures the depth into the target [19].

In the experimental setup the trajectories of the backscattered and sputtered particles which lie within the xy plane are of interest. Therefore $\gamma = 90°$ for these trajectories, and they can be described by θ as follows;

$$\theta = \psi + \beta \tag{3.1}$$

$$= \psi + |\arccos(\cos(\pm\beta))|\ . \tag{3.2}$$

The second line looks quite strange but remember that the $\cos\beta = \cos(-\beta)$ is given in the output files. the escape angle θ then has a range of $0 \leq \theta \leq 360°$, though in practice no particle would be found in $0 \leq \theta \leq \psi$ and $(\psi + 180°) \leq \theta \leq 360°$ since these particles don't leave the target. $\cos\gamma$ can then be used to limit the analysis to trajectories within the xy plane only. Except for the particle energy parameter, the other parameters in the output file are not necessary to perform an analysis on the energy-count distribution of these particles for different escape angles.

3.2.3 ▸ Limitations of SRIM

One big disadvantage of SRIM is that it does not take the charge of particles into account along with the effects of charge [2]. The projectile and target are

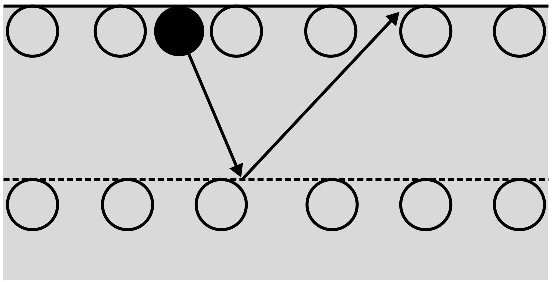

Figure 3.3: In SRIM the projectile starts on the surface layer [2]. If the particle has not been declared as having left the surface, it will be forced to have another collision [2].

treated as neutral. This could make the results of the simulation deviate from a real world experiment, along with other disadvantages such as the sensitivity of sputtering simulations to the surface binding energy, making it less reliable if there are uncertainties in surface binding energy [2, 16].

A big limitation of SRIM is that the projectiles start on the surface monolayer [2]. When using the Monolayer Collision Steps calculation method, this could introduce a side effect. The particle is only declared as a backscattered or sputtered particle if a succeeding collision would be above the surface, otherwise it would be forced to have another collision [2, 13]. This continues until it either does not have enough kinetic energy to displace another target atom, or is declared as backscattered or sputtered particle [2]. This situation is illustrated in figure 3.3.

3.3 ▶ SDTrimSP: Static and Dynamic Trim for Sequental and Parallel Computer

3.3.1 ▶ Introduction to SDTrimSP

The Static and Dynamic Trim for Sequental and Parallel Computer program, or *SDTrimSP*, is a Monte Carlo simulation program similar to TRIM [16, 17, 20]. However, it uses a Krypton-Carbon (Kr-C) interaction potential, but also allows for other potentials, such as ZBL, and other integration methods if specified [16, 17, 21]. SDTrimSP assumes that the target is at zero temperature, and like SRIM assumes that the target is amorphous [20]. SDTrimSP also allows for dynamic simulations such that stoichiometry and composition changes are made due to the sputtering and implantation of projectiles into the target [2, 16]. SDTrimSP a is more versatile program which allows for more input variables and input changes than SRIM, and more control over the output [2].

SDTrimSP provides much of the same input parameters SRIM provides [21]. Tables containing (standard) atomic and composition data among other things are included with SDTrimSP, which can also be altered to use different values from sources the user might desire to use. The parameters for controlling compound materials used for the SDTrimSP are more sophisticated than SRIM, along with how the simulation is performed and which calculation methods for various parts can be used. SDTrimSP also uses the same binding energy tables as SRIM [16].

SDTrimSP provides more output files and more output information. The backscattered and back sputtered particles are recorded in the *partic_back_p.dat* and *partic_back_r.dat* files respectively. Similarly to SRIM, SDTrimSP records the output trajectory with angles, but notably uses polar and azimuthal angles instead [22]. The variables stored in the output files for SDTrimSP are the cosines of the polar and azimuthal angles. The azimuthal angle is defined to be $0°$ at the surface normal. These values can be converted to $\cos\alpha$, $\cos\beta$ and $\cos\gamma$ such that the trajectories can be analysed similarly to how they are analysed for SRIM. Then only the energy parameter and the polar & azimuthal angle parameters from the output files of SDTrimSP are needed to make an analysis of the energy-count distribution of the backscattered and sputtered patricles for different escape angles.

Compared to SRIM, SDTrimSP is a versatile package to simulate sputtered particles [16]. Certain limitations of SRIM are solved with the SDTrimSP package, such as the starting point of the incident trajectory. For SRIM it starts on the surface but for SDTrimSP it starts 2.2 Å above the surface [2]. In SRIM the charge is not taken into account [2], while for SDTrimSP it seems that the charge of the projectiles is zero if fixed beam energies are used [21]. However, for SDTrimSP it was somewhat unclear just from Mutzke, Schneider, Eckstein, Dohmen, Schmid, von Toussaint, and Badelow [21].

It was found from other simulations that SDTrimSP is in reasonably good agreement with experiments whereas SRIM tends to disagree more [16, 17]. It seemed that the ZBL potential model was limited in characterizing low energy collisions, while the Kr-C model seemed to be in reasonably good agreement with experiments in comparison [17]. However, SRIM would still show worse agreement even if the same interaction potentials were used [17].

Chapter 4 Sn Ion Interactions with $4d^n$ Elements

In the previous chapters the foundations were set to better understand the setup of ions from a beam interacting with a solid target, and how they can be simulated using SRIM and SDTrimSP. This was then used to conduct simulations of 14 KeV Sn ions on $4d^n$ solid targets with an angle of incidence of $\tilde{\psi} = 5°$ from the surface normal to analyse the energy-count distribution for different escape angles for backwards sputtered particles specifically for each target and simulation program, and to make comparisons between them. In this chapter, these simulations are described, along with how they were performed and a discussion on the results.

4.1 ▸ Simulation Setup

4.1.1 ▸ Introduction to the Simulation

The simulation presented in this work is according to the general setup as described in chapter 3; about two million 14 KeV Sn ions were simulated to bombard a solid target at a $\tilde{\psi} = 5°$ angle of incidence (corresponding to $\psi = 85°$) to obtain energy-count distributions for different escape angles θ for sputtered particles specifically. In particular, the Sn ions were ^{120}Sn isotopes. This simulation was performed for ten different target solids. These targets are the elements for which the ground electron configuration contains the unfilled $4d^n$ subshell. Cd is simulated too, for which the subshell is actually filled. Therefore the elements used for the simulations are listed in table 4.1. These elements were chosen specifically since they have similar electron configurations, masses and standard atomic weights. Comparisons could be made between the results of the simulations for each target to understand how relatively little differences in elements would influence the energy-count distributions of the backwards sputtered particles.

SRIM and SDTrimSP were the programs used for the simulations. SRIM ran on a laptop and desktop computer, while SDTrimSP ran on a high performance supercluster. The details of these programs were discussed before in chapter 3. With these simulations the results of SRIM and SDTrimSP will be compared to understand how they perform for these elements.

Element	Ground Electron Configuration
Y	[Kr] 4d $5s^2$
Zr	[Kr] $4d^2$ $5s^2$
Nb	[Kr] $4d^4$ 5s
Mo	[Kr] $4d^5$ 5s
Tc	[Kr] $4d^5$ $5s^2$
Ru	[Kr] $4d^7$ 5s
Rh	[Kr] $4d^8$ 5s
Pd	[Kr] $4d^{10}$
Ag	[Kr] $4d^{10}5s$
Cd	[Kr] $4d^{10}5s^2$

Table 4.1: Table containing the target elements used in the simulations along with their chemical symbol and ground electron configuration. Configuration data from NIST [4].

4.1.2 ► Simulation Properties and Parameters

Many simulation parameters can be specified in SRIM and SDTrimSP. To start off, the following properties were specified for the ion beam;

Element	Fixed Energy	Angle of Incidence
^{120}Sn	$E_0 = 14$ keV	$\tilde{\psi} = 5°$ ($\psi = 85°$)

The initial energy value of $E_0 = 14$ was chosen based on the simulations previously performed in the paper Deuzeman [2] and would seem like a natural starting point. $\tilde{\psi} = 5°$ was chosen to understand how an incident trajectory close to the surface normal would influence the sputtering from the target.

In SRIM it was simple to specify the mass of the element, and 119.902 u was used to reflect the use of the ^{120}Sn isotope. After testing, it proved to be difficult to use this exact isotope for the beam with SDTrimSP, since the program kept reporting 'FAILED' when using the 'a_mass' parameter, with which the masses of the elements could manually be specified [21]. The reason why the simulations failed remained unknown. Therefore the mass value of 118.710 u from the program's *table1* was used (the included table SDTrimSP uses element data from by default), which is actually the standard atomic weight for Sn [21, 23]. Certain input parameters for SDTrimSP would allow for the use of the single isotope, however it was difficult to make the program function properly with this and it was argued that this little mass difference might be not as significant to the simulation and comparison. However, this is where the simulations could have definitely improved already. SDTrimSP allows for users to alter the contents *table1* such that SDTrimSP could use values required by the user. This particular method was not tested but it could be a possible solution to the problem.

The solid targets were made up of just the pure elements by themselves, but the choice was made to take into account the natural abundance of these elements' stable isotopes when preparing the target composition for the simulations. This is because it would create a more realistic scenario compared to preparing a target composed of only a single isotope. In SRIM this was done by preparing a layer consisting of the stable or most abundant isotopes with their masses and composition data from Coursey, Schwab, Tsai, and Dragoset [23] and Rumble [24]. This posed a problem for Tc, since no natural abundance data was available. It was chosen to use the ^{98}Tc isotope to make up the target material for that element since it has the longest half-life time [24].

Contrary to the simulations with SRIM, the natural isotopic composition was not taken into account with SDTrimSP, and the data from *table1* was also used for the target material, since it proved to be difficult to construct a functioning composition similar to SRIM. A flag could be set with the 'isot' parameter such that SDTrimSP would use program's *table2*, which takes the isotope masses with their natural abundances into account. However, 'FAILED' reports were returned as well, similarly to before when using the 'a_mass' parameter. This would also be an area for improvement by investigating how this parameter can be used properly.

For SRIM the layer density values were obtained from Rumble [24]. The internal tables from SDTrimSP were used for its simulations however. A target width of 50 Å was used for SRIM while a width of 5000 Å was used for SDTrimSP. This was because the full dynamic calculation was used with SDTrimSP, which would change the composition of the material due to sputtering, while SRIM recommends lower widths such as 50 Å mentioning that it is adequete [2, 18]. 5000 Å was also used in the simulations from Noordam [3] for SDTrimSP. Other target-specific parameters were left to default.

To determine whether 50 Å for SRIM was suitable, a small test was performed with Sn on Zr with layer widths of 20 Å, 30 Å, 50 Å, 80 Å, 100 Å, and 5000 Å to see how many sputtered particles would be found. $10,000$ ions were used for this test. Only one simulation was performed for each layer width, therefore making the test not statistically conclusive. However, it could function as a small indication whether on the suitability of certain layer widths. The data obtained was normalized by their highest number of counts over all widths. The results are depicted in figure 4.1. It can be seen that the plot shows little difference in the number of counts between 50 Å and 100 Å , while the difference between 100 Å and 5000 Å is a little larger but also relatively small. Below 50 Å the number of sputter counts reduces more dramatically. Since SRIM recommends layer widths of 40 Å to 50 Å for heavier targets and efficiency, 50 Å was chosen for the SRIM simulations [18].

For SRIM, it was chosen to simulate $2,000,000$ ions. It was expected that this would provide sufficient statistics for analysis. The Monolayer Collision Steps method was used since it was suggested that this calculation method was essential for sputtering application [13]. For SDTrimSP it was chosen to simulate $2,000,040$ ions. This is because it was chosen to have sixty projectiles between target update, similarly to the simulations from Noordam [3]. The total number of projectiles is a multiple of this number, making $2,000,040$ the closest number to two million

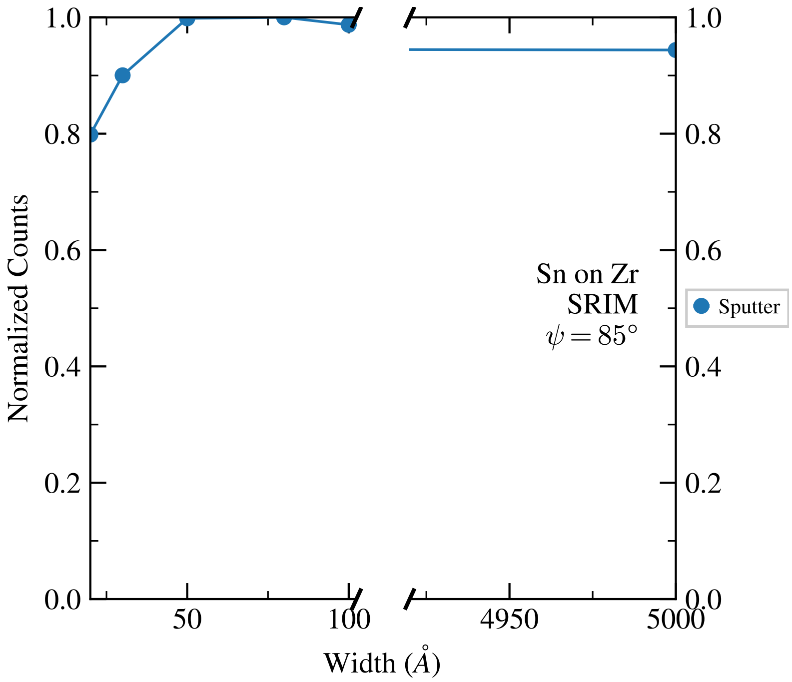

Figure 4.1: This figure shows the number of sputter counts for layer widths of 20 Å, 30 Å, 50 Å, 80 Å, 100 Å, and 5000 Å for Sn on Zr. Only one simulation was performed for each layer width, reducing the conclusiveness. However it can still be a somewhat useful indicator.

while still being above two million [21]. In hindsight $1,999,980$, which is closer to two million overall, was probably a better choice since it might not be as significant to use more than $2,000,000$ projectiles.

Since SRIM uses the ZBL potential, it was specified to use the ZBL potential with SDTrimSP as well, which could make for a better comparison between the two programs. For the surface binding energy calculation method, the third option mentioned in Mutzke, Schneider, Eckstein, Dohmen, Schmid, von Toussaint, and Badelow [21] was used, along with the Gauss-Mehler quadrature integration method, which was recommended for the number of integration-steps being larger than 8 [21].

4.1.3 ▸ Processing Details

For the data analysis, the *SPUTTER.txt* and *partic_back_r.dat* were processed from SRIM and SDTrimSP respectively. These files can become really large for the number of ions used in the simulation. Therefore the files were processed in chunks, which made it more easy for the computer to handle.

For an energy-count distribution analysis, only the energy and angle parameters were of use. The $\cos\alpha$, $\cos\beta$ and $\cos\gamma$ angles were used in processing the data.

This meant that the polar and azimuthal angle SDTrimSP uses had to be converted.

For this simulation, only the trajectories of the sputtered particles which lie in the same plane as the incident beam trajectory, the xy plane, were of interest. Therefore the particles which don't have $\gamma = 90°$ would be filtered out. However, rarely any particle would have exactly this angle in comparison. Therefore a band of $\Delta\gamma = 3°$ around $\gamma = 90°$ was used to be able to keep enough statistics. This was done by imposing the following check;

$$|\cos\gamma| \leq \cos 87° = \sin 3° \,. \tag{4.1}$$

Only the particles for which this holds true were kept.

Then the particles were filtered by their escape angle. To again keep enough statistics, a band of $\Delta\theta = 1°$ was chosen. This was done by imposing the following check;

$$(\theta - 1) < (\arccos(\cos\beta) + \psi) < (\theta + 1) \,, \tag{4.2}$$

which might look strange but remember that $\cos\beta$ is the value provided by the output. One thing to keep in mind with this check is that it does not filter based on a solid angle cone around the escape angle due to $\Delta\gamma$ band imposed before. Recall that the escape angle is the angle between the extended trajectory of the incident ion and the trajectory of the sputtered particle. In 3D space the sputtering trajectory does not necessarily lie exactly within the xy plane, since the $\Delta\gamma$ band was imposed. Rather than obtaining a solid angle cone, a long pyramid like shape is obtained instead centered around the escape angle in the xy plane. It was assumed that this difference would not be of great significance to the analysis of the simulations. However, it might be important to keep in mind.

Then the energy of the remaining particles would have to be categorised to be able to create a distribution. This was done by using energy bins of $\Delta E = 1$ eV. This categorisation was performed by imposing the following check;

$$N\Delta E - 0.5\text{ eV} < E_i < N\Delta E + 0.5\text{ eV} \,, \tag{4.3}$$

where E_i is the energy of the particle which is currently checked and $N = 0, 1, 2, 3, \ldots, N_{\text{max}}$ is the bin number. N_{max} corresponds to the energy bin containing the particles of the largest amount of energy. This check was performed by scanning N for each particle individually until this condition was satisfied, after which that particular particle was added to the corresponding bin. After this categorisation the data is stored in a new file which is ready for analysis. For each target, the energy-count distributions were obtained for the escape angles $90° \leq \theta \leq 260°$ in steps of $5°$.

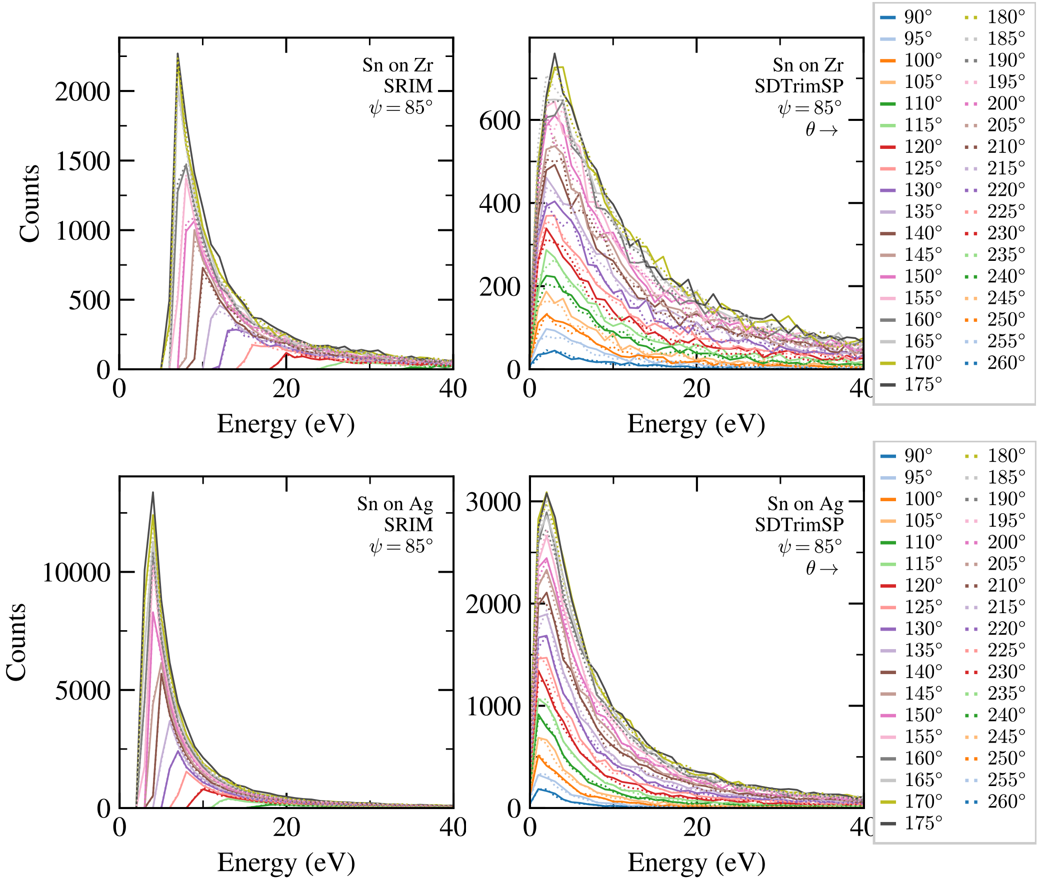

Figure 4.2: Energy-count distribution plots for both SRIM and SDTrimSP sputtering simulations for Sn ions on Zr and Ag targets. The energy of the Sn ions is 14 KeV and the angle of inidence is $5°$. These graphs show a distribution line for each escape angle θ. Note that the distribution line is dotted if the corresponding θ is higher than the angle corresponding to the surface normal.

4.2 ▸ Simulation Results

4.2.1 ▸ Data Analysis on Backwards Sputtered Particles

First of all, a large quantity of plots were obtained for the simulations of 14 KeV Sn impinging on 4d$^{\mathrm{n}}$ solid targets with an angle of incidence of $\tilde{\psi} = 5°$ (corresponding to $\psi = 85°$). The energy-count distribution, energy peak & cutoff, and count peak over escape angle graphs for each target can be found in appendix A. It may be useful to consult the appendix since many graphs can not be included within this chapter. In this discussion mostly Zr and Ag graphs will be included to keep consistency among the figures. However, comparisons are made between plots from different targets which are not all shown in this chapter. Please refer to appendixA.

Element	SRIM	SDTrimSP
Y	506,836	691,184
Zr	561,661	628,915
Nb	579,784	630,042
Mo	865,405	745,461
Tc	3,753,476	794,206
Ru	1,278,014	869,983
Rh	1,639,796	961,593
Pd	2,207,991	1,293,636
Ag	2,149,947	1,508,712
Cd	4,686,675	2,705,348

Table 4.2: Total number of counts for which $\gamma = (90 \pm 3)^\circ$ for each simulation program and target.

The energy-count distributions plots for backwards sputtered particles will be discussed first. For Zr and Ag, two such figures, one for each simulation program, are shown in figure 4.2. A few things are immediately evident. The energies of most sputtered particles are very low compared to the initial energy. For SRIM, which ran on a laptop and desktop computer, most sputtered particles found generally have energies between about 5 eV and 20 eV, while for SDTrimSP, which ran on a high performance supercluster, most sputtered particles have energies between 0 eV and about 40 eV.

It can be observed that the energy plots have peaks. The peaks in the SRIM graphs seem to increase in counts and to shift to lower energies as the escape angle increases, up until the escape angle would correspond to the surface normal. This would be at $\theta = \psi + 90^\circ = 175^\circ$. After this angle the peaks move back to higher energies, and decrease in the number of counts. Notable is also that the number of counts at these peaks increases drastically as θ increases until $\theta = 175^\circ$, after which it also declines similarly to the peaks shifting back to higher energies.

The energy-count distribution can be observed to be symmetric around the surface normal, similar to simulations discussed in Hofsäss, Zhang, and Mutzke [16]. This seems to be the case for every solid target which was simulated. Comparing this to SDTrimSP, the energy-count graphs obtained with this program do not show this shifting behaviour at all. The count peaks seem to stay at more or less the same energy for any θ. The number of counts of the peaks themselves seem to also be mirrored around the angle corresponding to the surface normal.

Speaking of counts, it seems that SRIM counted way more sputtered particles around the peak energies than SDTrimSP did. This seems evident from the y-axis scaling. However, the shapes of the plots in both figures differ; The SDTrimSP plots are much broader than the plots from SRIM, and therefore more sputtered particles are more spread out over energy. In fact, the number of sputtered particles for which $\gamma = (90 \pm 3)^\circ$ over all θ for each element is presented in table 4.2. It

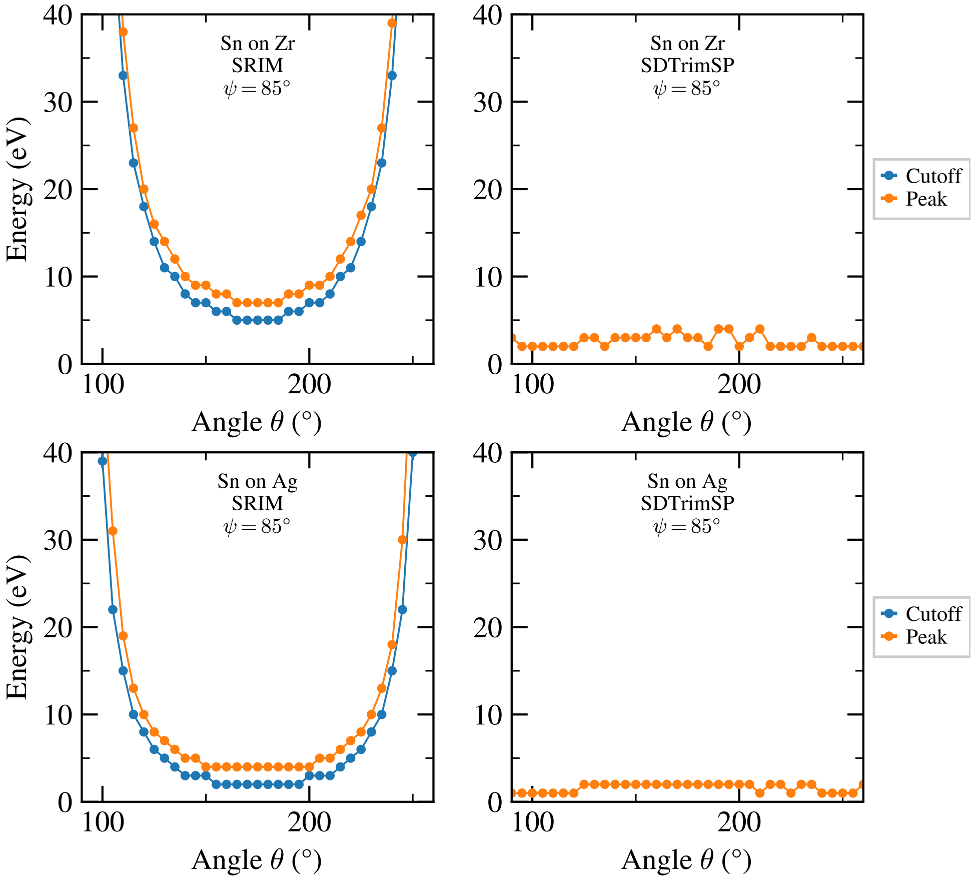

Figure 4.3: Plots showing the energy peak and cutoff against the escape angle θ for Sn on Zr and Ag. The SRIM plots seems to be mirrored around the surface normal. The SDTrimSP graph does not appear to have a cutoff at all, while the peak energy line is almost flat.

can be seen that SDTrimSP finds more sputtered particle counts for the lightest three elements than SRIM does. SRIM finds more counts for all the other elements. Very notable is Tc, which seems like an outlier here. Recall however that Tc was a special case considering its natural abundance and stability. Another observation is the general trend of increasing number of counts for heavier elements for both the SRIM and SDTrimSP simulations. This is evident from table 4.2 and the plots. It also seems that for both simulations, the plots become shallower for heavier targets.

The SRIM graphs show some kind of cutoff close to the peaks. For the Zr plots for example, the lowest amount of energy found from a sputtered particle was around 5 eV. For the plots corresponding to angles further from the surface normal, this cutoff also increases in energy slowly, similarly to how the peaks shift to higher energies. To show this effect better, plots shown in figure 4.3 were made for each target. It appears that these peaks and cutoffs seem to be different for each target.

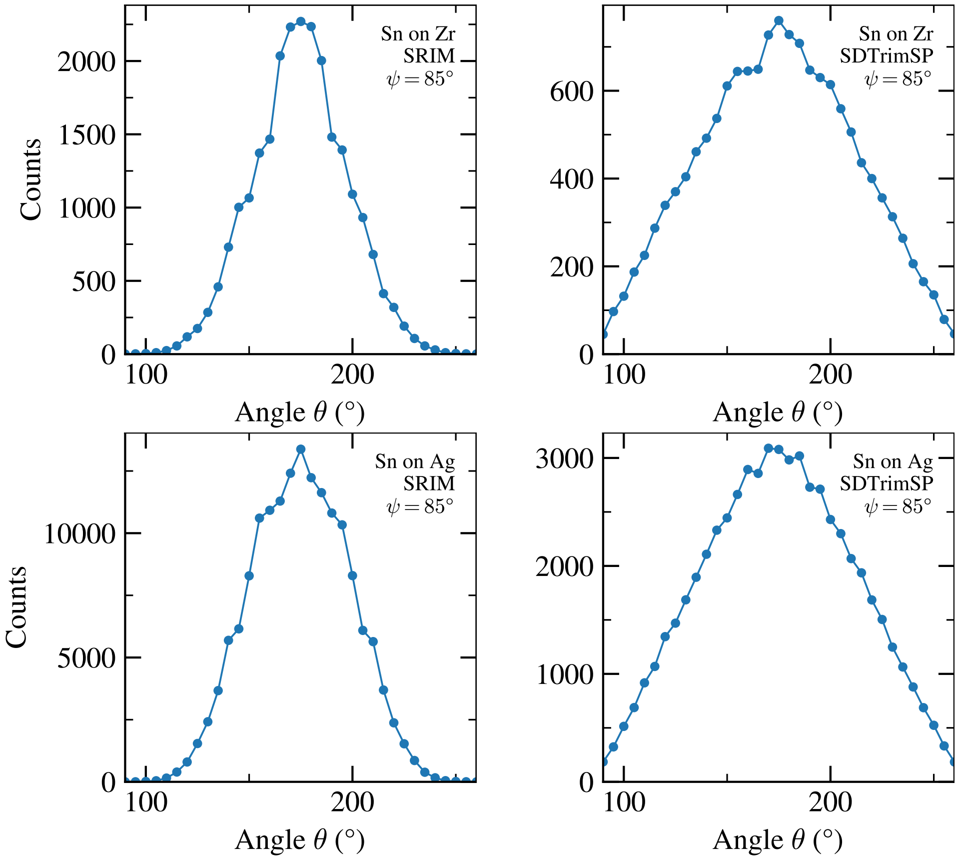

Figure 4.4: Plots showing the number of counts at the peaks against the escape angle θ for Sn on Zr and Ag. Both plots seem to more or less be mirrored around the surface normal.

They all follow a similar shape, however the energies at which they are located are different. The plots from SDTrimSP do not have any cutoff at all, and it is again evident that the peaks all roughly have similar energies over θ.

When looking at the plots showing the number of counts at the peak versus θ, a few of which are shown in figure 4.4, it can be observed that the plots for SRIM take somewhat of a Gaussian-distribution-like shape, whereas SDTrimSP seems to take more of a $C - D|\theta - 175|$ shape, were C and D are constants, though for some targets it seems to flatten out a bit near the surface normal.

4.2.2 ▶ Discussion

It was evident that the results for each simulation program and target were symmetric around the surface normal $\theta = 175°$. For the SRIM plots this symmetric behaviour around the surface normal seems to be in agreement with what was found in Hofsäss, Zhang, and Mutzke [16], but not necessarily for the SDTrimSP plots. Perhaps this

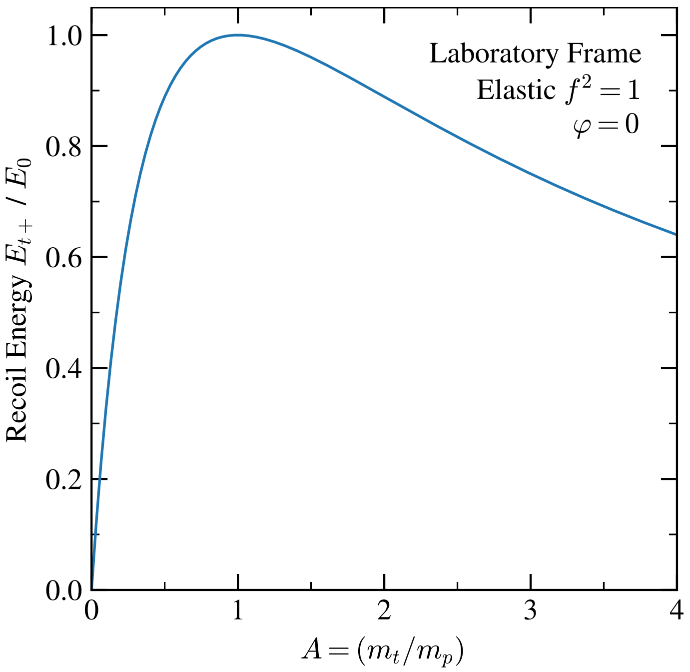

Figure 4.5: This figure illustrates the amplitude of the recoil energy in the laboratory frame. The amplitude was plotted by using the recoil energy with a recoil angle of $\varphi = 0$ for an elastic collision, essentially plotting the behaviour of $A/(1+A)$. It is evident that the amplitude increases as the target mass approaches the projectile mass, since the maximum is at $A = 1$.

might be due to the incident angle of $\tilde{\psi} = 5°$ being rather small such that the incident ions are bombarding the target at nearly the surface normal. This could have been more conclusive if more simulations were performed with variations in incident angles as well. By using just simulating one incident angle the effects it may have would not be properly understood, plus any observations made in the plots in appendix A can not easily be related to the incident angle.

From table 4.2 it was evident that the number of counts for which $\gamma = (90 \pm 3)°$ increases as the targets mass increases. This trend could be investigated by looking at the amplitude of the recoil energy in the laboratory frame, seen in equation 2.15. As $m_t \to m_p$, $A/(1+A)$ increases as illustrated in figure 4.5. One idea could be that perhaps a larger cascade could be induced due to the larger amount of recoil energy available from the increased amplitude, therefore potentially have more particles leave the target. The mass differences between each target is not large. However, since two million ions were simulated, this difference could statistically build up into a more significant difference in counts found within $\Delta\gamma$. This is not completely conclusive since this behaviour was not further investigated, nor was this analysed for all counts (including the ones outside of $\Delta\gamma$). This was simply a line of thought which could be beneficial to investigate in future analysis.

During the analysis, it was not exactly clear why the peaks in the energy-count distributions for SRIM are shifting in θ . This is also somewhat paired with the cutoff shifting to higher energies for angles further away from the the angle corresponding to the surface normal. At least no trend which would depend on the density or mass could be observed for the energies of the peaks and cutoffs. SDTrimSP did not show this behaviour at all for reasons which were not clear. The only trend regarding the peaks from the SDTrimSP plots is that the peak energies are generally lower for the heaviest targets, but the peaks and cutoff energies do not shift over θ. It could be suggested that the energy cutoff might represent the energy a sputtered particle might need at minimum to be able to escape the target, which would in turn not explain why SDTrimSP does not show this peak and cutoff shifting behaviour. Perhaps more simulations could have been performed with different input parameters to investigate if this behaviour changes depending on certain input variables.

It is also not exactly clear why the number of counts for Tc in the SRIM simulation seem like outliers, while they seem like they follow the general trend for SDTrimSP simulations. Tc is the only element used as a target which does not have a stable isotope [23, 24]. It is unlikely that this has something to do with the mass used in the simulations, since a mass of 97.91 u was used for SRIM, more or less in between the lowest and highest masses used in the simulation. It could be due to the composition, since a layer of only a single isotope with this mass was used with SRIM, while the other targets had a more sophisticated composition based on Coursey, Schwab, Tsai, and Dragoset [23]. Tc did not seem to be an outlier in the SDTrimSP plots. In SDTrimSP, the target information from the tables that come with the program were used for simulations on each target, which makes the simulations more coherent within SDTrimSP.

The Monolayer Collision Steps / Surface Sputtering calculation method from SRIM is sensitive to the surface binding energy [13]. The reason Tc is an outlier only for SRIM could also be because of the surface binding energy. The surface binding energy of an atom to a surface is only known for a few materials, making it therefore common to use the heat of sublimation as an approximation [18]. It was also mentioned that the value of the surface binding energy is sometimes difficult to estimate [13]. Since comparatively less seems to be known about the thermodynamic properties of Tc, this could perhaps lead to problems when using SRIM to simulate sputtering of Tc [24]. Perhaps not enough is known about the surface binding energy or other thermodynamic parameters of Tc such that Tc is an outlier in the SRIM simulation. These properties for Tc were not investigated enough, along with this reasoning however, which is where this investigation could have been improved. Therefore this reasoning is not conclusive enough.

Moreover, Instead of using beam and target compositions identical to SRIM with SDTrimSP, only the mass data from *table1* was used with it, making the masses function more like standard atomic weight rather than working with individual isotopes and/or compositions [21]. The simulations could have been improved by altering the contents of *table1* and altering the input parameters to prepare a proper solid target composition.

Interpretation of these results is limited however. In section 4.1.2, certain limiting factors for these simulations were already mentioned. Recall that SRIM does not take charge into account, neither does it start the simulation with the projectile above the surface monolayer [2]. Certain trends, or the lack of them, could possibly be explained because of this. However, this was not further investigated, but the analysis could have been improved if it was. Another point previously mentioned is the check on θ. The check now filters based on more of a pyramid shape rather than a solid angle cone. It is not necessarily a big limitation, but it is something important to keep in mind.

Above all, there was no experimental data available for comparison with the simulations, so it is difficult to make qualitative conclusions on the realism of these results, although other simulations have proven that SDTrimSP is usually in good agreement with experiments, while SRIM seems limited and performs less well [16, 17].

Chapter 5 Conclusions

In this thesis the backwards sputtered particles from 14 KeV ^{120}Sn ions interacting with 4d$^{\mathrm{n}}$ solid targets at an angle of incidence of $5°$ from the surface normal were investigated using the simulation programs SRIM and SDTrimSP. To get a better understanding of the basic principles behind projectile-target collisions, a binary collision was treated in its basic form. Then the simulation setup was discussed along with an introduction on SRIM & SDTrimSP, as well as their limitations and comparisons between the two. Finally, the details on Sn simulations on 4d$^{\mathrm{n}}$ targets were explained, along with their results, which were discussed with limitations in mind.

5.1 ▸ Binary Collisions

When a projectile collides with a stationary target atom, it loses kinetic energy and scatters with a *scattering angle* ϑ [5]. From the conservation of energy and momentum, it can be deduced that the projectile's *scattering energy* after the collision in the laboratory frame is given by [5];

$$\frac{E_{p\pm}}{E_0} = \left(\frac{\cos\vartheta \pm \sqrt{(Af)^2 - \sin^2\vartheta}}{1+A} \right)^2 , \tag{5.1}$$

where E_0 is the projectile's initial energy, $A = m_t/m_p$ and $f^2 = 1 - \frac{1+A}{A}\frac{Q}{E_0}$. This in general takes into account inelastic energy loss. $f^2 = 1$ for elastic collisions [5]. If $Af < 1$, both the positive and negative signs are valid, while only the positive sign is valid if $Af \geq 1$ [5]. This becomes evident when constructing *Newton diagrams* of the system. If $Af < 1$, a *maximum scattering angle* ϑ_{max} exists;

$$\vartheta_{\text{max}} = \pm \arcsin{(Af)} \, . \tag{5.2}$$

The recoiled target particle gains kinetic energy after the collision. Its *recoil energy* after the collision in the laboratory frame is given by [5];

$$\frac{E_{t\pm}}{E_0} = A \left(\frac{\cos\varphi \pm \sqrt{f^2 - \sin^2\varphi}}{1+A} \right)^2 , \tag{5.3}$$

where φ is the *recoil angle*. If the collision is elastic, only the solution with the positive sign exists.

Recursive application if the single binary collision forms the basis of the *Binary Collision Approximation*, which forms the basis for many simulation programs [5].

5.2 ▸ Simulation Programs

When an ion projectile penetrates a solid target, a few things can happen. Firstly, the projectiles can *backscatter*, meaning they leave the target again after the interactions. This can be either after 1 collision or after many collisions, the former being referred to as *single scattering* [2]. The projectile can cause a *cascade*, which could lead to recoiled target atoms leaving the solid target if they have enough kinetic energy [2]. Target atoms leaving the solid due to projectile penetration is referred to as *sputtering* [5, 11]. When the target atom specifically leaves from the surface the projectile penetrated it is referred to as *backwards sputtering* [2].

SRIM and *SDTrimSP* are simulation programs which can simulate projectiles penetrating targets and record information on backscattered and sputtered particles [2, 16, 19, 21]. Both simulations can use the ZBL potential. SDTrimSP is a more versatile program compared to SRIM, which is often considered as rather limited [16, 17]. SRIM does not consider charge in its simulations and starts the trajectory of the projectile below the surface monolayer, while SDTrimSP seems to use a charge of zero for fixed projectile energies and starts the trajectory above the surface [2, 21]. SDTrimSP also allows for more input parameters and records a more comprehensive output [21].

5.3 ▸ Sn ions on $4d^n$ targets

SRIM and SDTrimSP simulations were performed for 14 KeV ^{120}Sn ions interacting with $4d^n$ elements. This includes elements from Y to Cd [4]. About two million ions were simulated to penetrate the targets at a $5°$ angle of incidence, which is near the surface normal. The energy-count distributions of the backwards sputtered particles somewhat within the xy plane were analysed for various escape angles ranging from $90°$ to $260°$.

For both simulation programs, it was found that most sputtered particles had low energies. In particular, most sputtered particles generally had energies between about 5 eV and about 10 eV for SRIM and between 0 eV and about 40 eV for SDTrimSP. For SRIM it was found that for every target element, the peaks in the plots shifted to lower energies as θ approaches $175°$, which corresponds to the surface normal, while the plots for SDTrimSP did not show this behaviour. It seemed that simulations for both programs showed the mirroring of distributions around the surface normal, which for SRIM is in agreement with [11].

An energy cutoff was observed for the SRIM plots which shifted in a similar manner as the peaks, while SDTrimSP did not show any energy cutoffs. It is unclear why SRIM showed this behaviour, though it could be suggested that the energy cutoff is representative of the energy the particle might need to escape the material, however SDTrimSP does not show this behaviour, making the problem left somewhat unexplained.

A general trend was observed in the increasing number of counts as the targets become heavier. An idea of why this is the case could be that this is due to the amplitude of the recoil energy, which increases as the mass of the target approaches the mass of the projectile, such that a larger cascade could perhaps be induced. This might then increase the number of sputtered particles. However, this idea was not further investigated. Notable though is that SRIM counted much more sputtered particles than SDTrimSP did for the heavier targets. Only for the lightest three targets did SDTrimSP find more particles.

The simulations could have been improved by using the exactly same beam and target compositions, which proved to be difficult to perform properly. This way, more qualitative comparisons could be made between SDTrimSP and SRIM. More different incident angles could also be simulated to obtain a better understanding of the distribution mirroring.

Above all however, no comparisons were made with experimental data, which could improve qualitative conclusions in how SRIM and SDTrimSP perform, although it has been proven with other simulations that SDTrimSP is more in agreement with experiments than SRIM [16, 17].

Chapter A Sn Simulation Plots

All significant plots made from the simulation data are shown below, categorised by the solid target material. Discussion on these plots is written in chapter 4. The number of graphs was too large to show them all within that chapter. Some graphs can still be found there for easier reference during the discussion, however this appendix can be referenced when comparing more plots.

A.1 ▸ Y

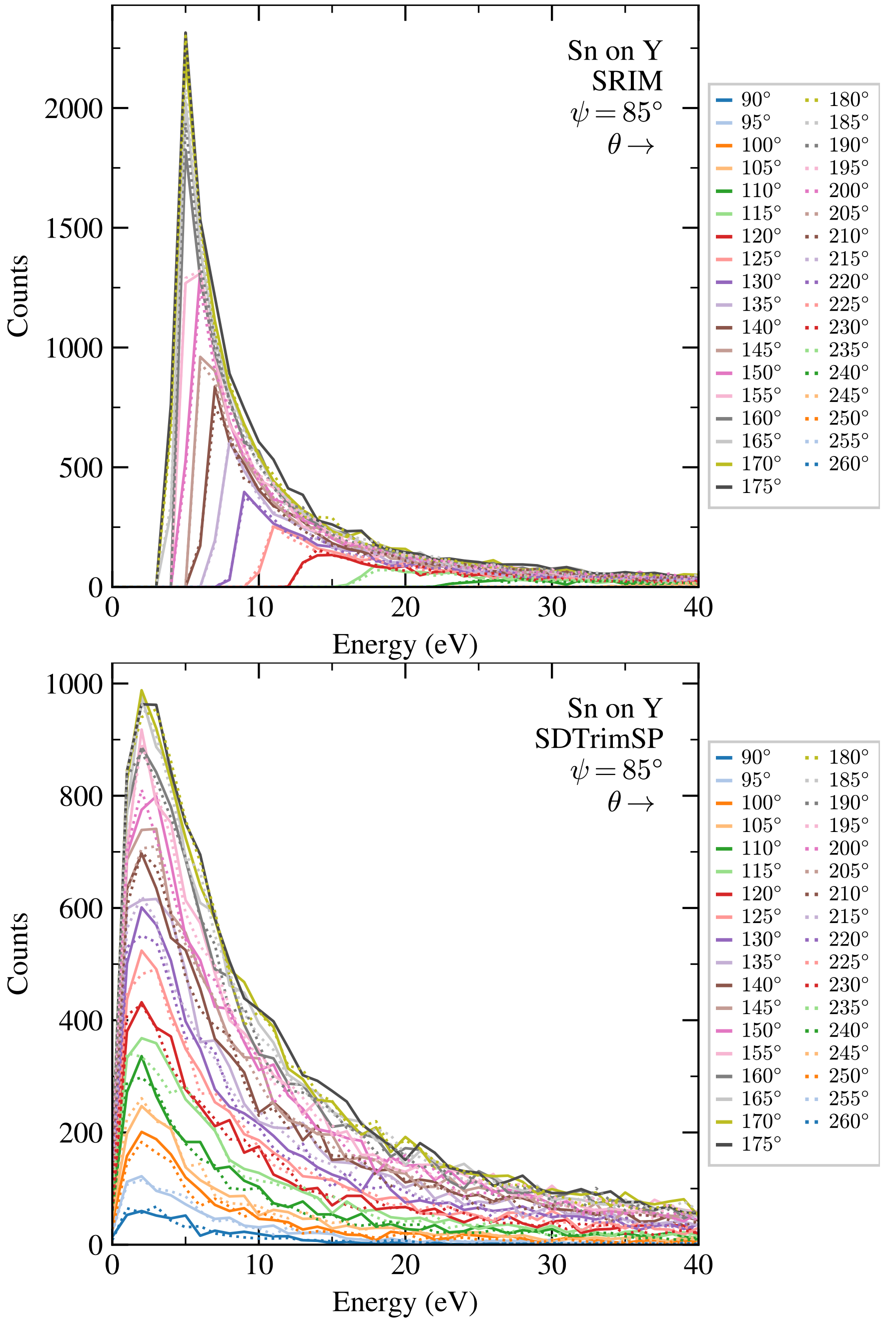

Figure A.1: Energy-count distribution plots comparing SRIM with SDTrimSP for different escape angles θ .

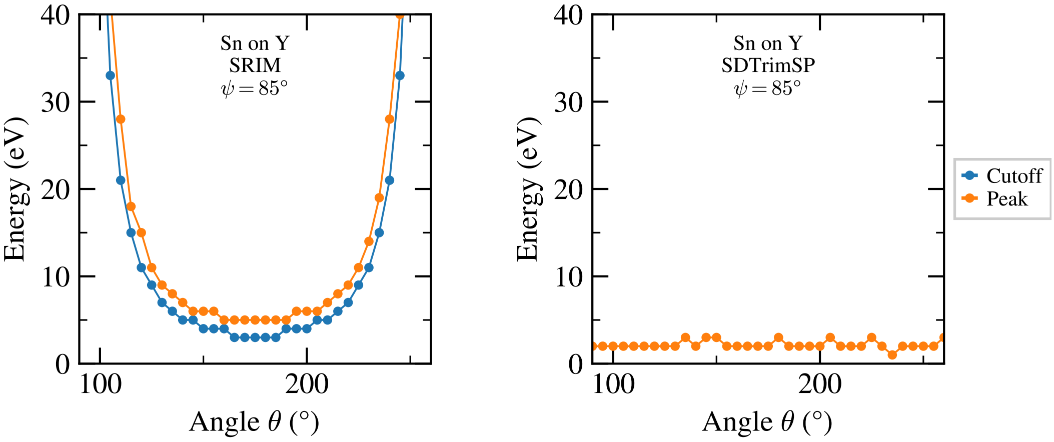

Figure A.2: Plots showing the energy peak and cutoff against the escape angle θ .

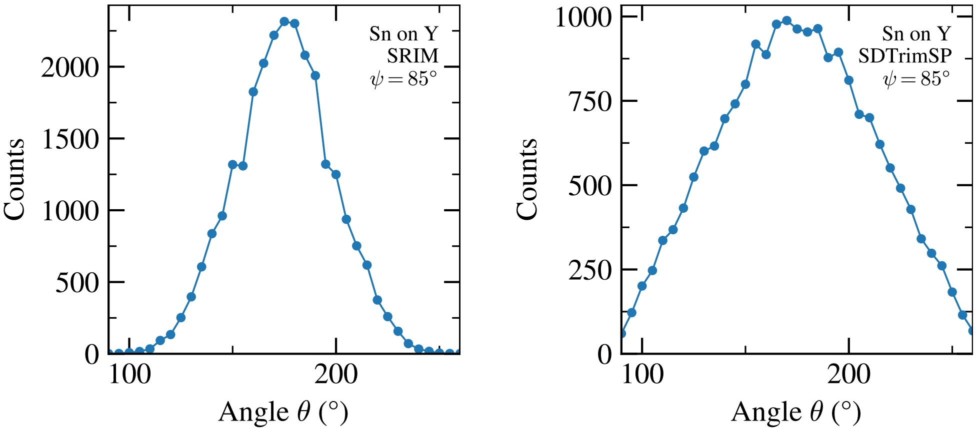

Figure A.3: Plots showing the energy peak count against the escape angle θ . The count peak in the SRIM diagram seems to be around 175° .

A.2 ► Zr

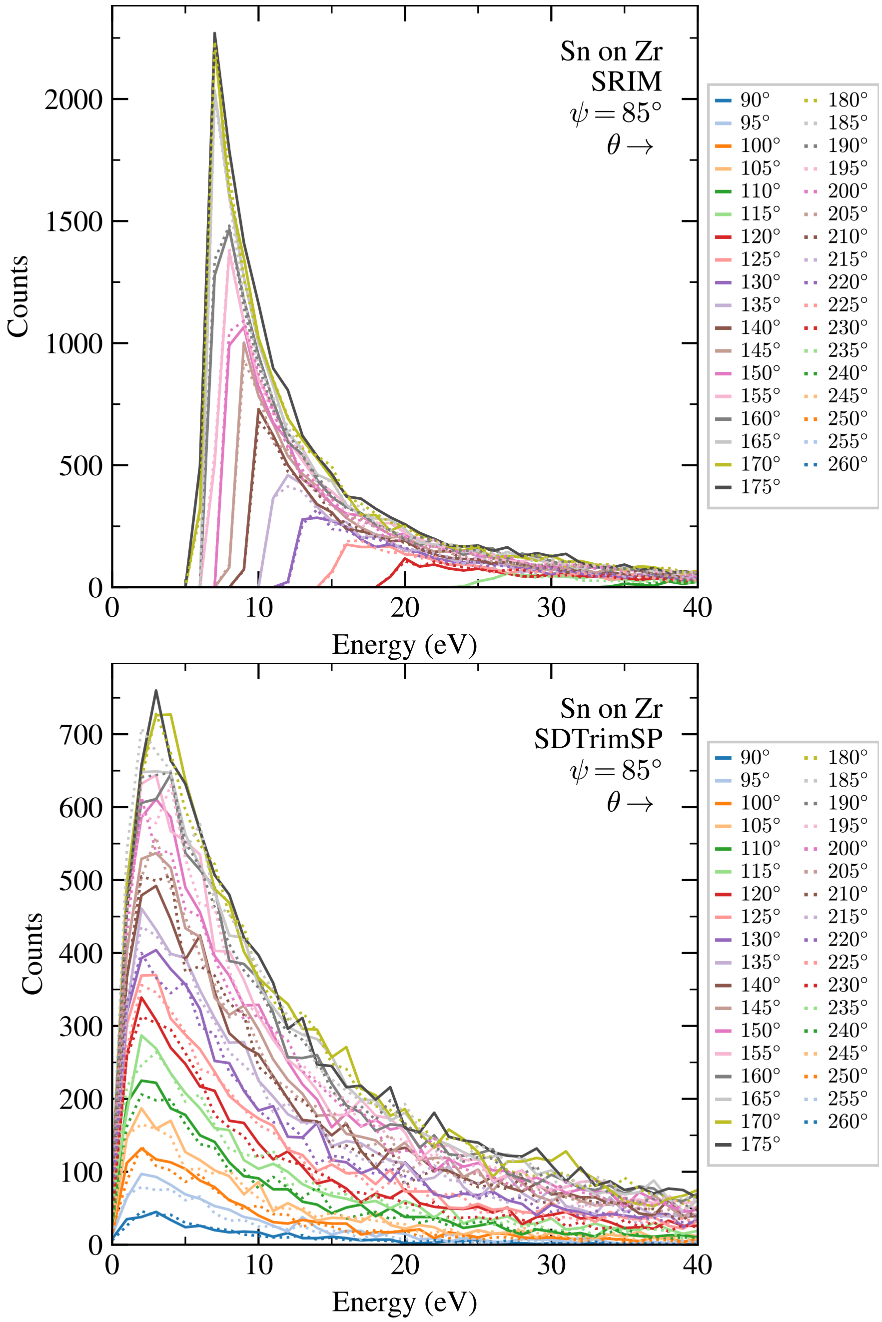

Figure A.4: Energy-count distribution plots comparing SRIM with SDTrimSP for different escape angles θ .

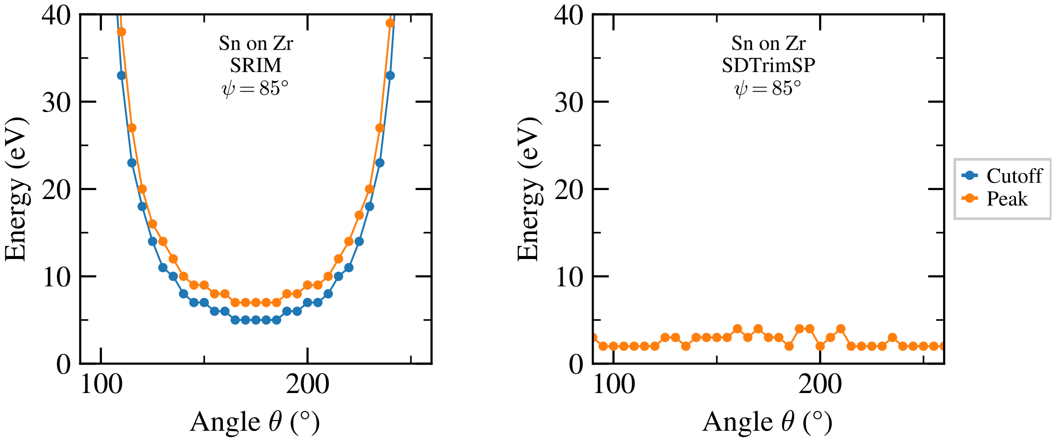

Figure A.5: Plots showing the energy peak and cutoff against the escape angle θ .

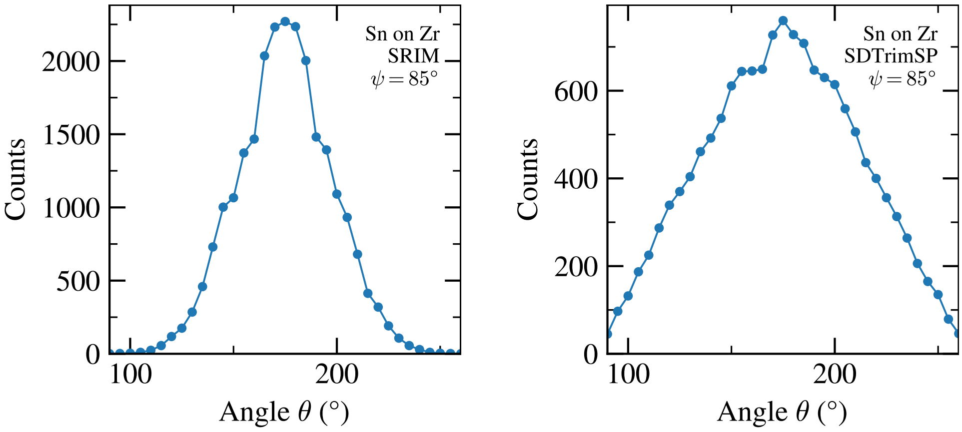

Figure A.6: Plots showing the energy peak count against the escape angle θ . The count peak in the SRIM diagram seems to be around 175° .

A.3 ▸ Nb

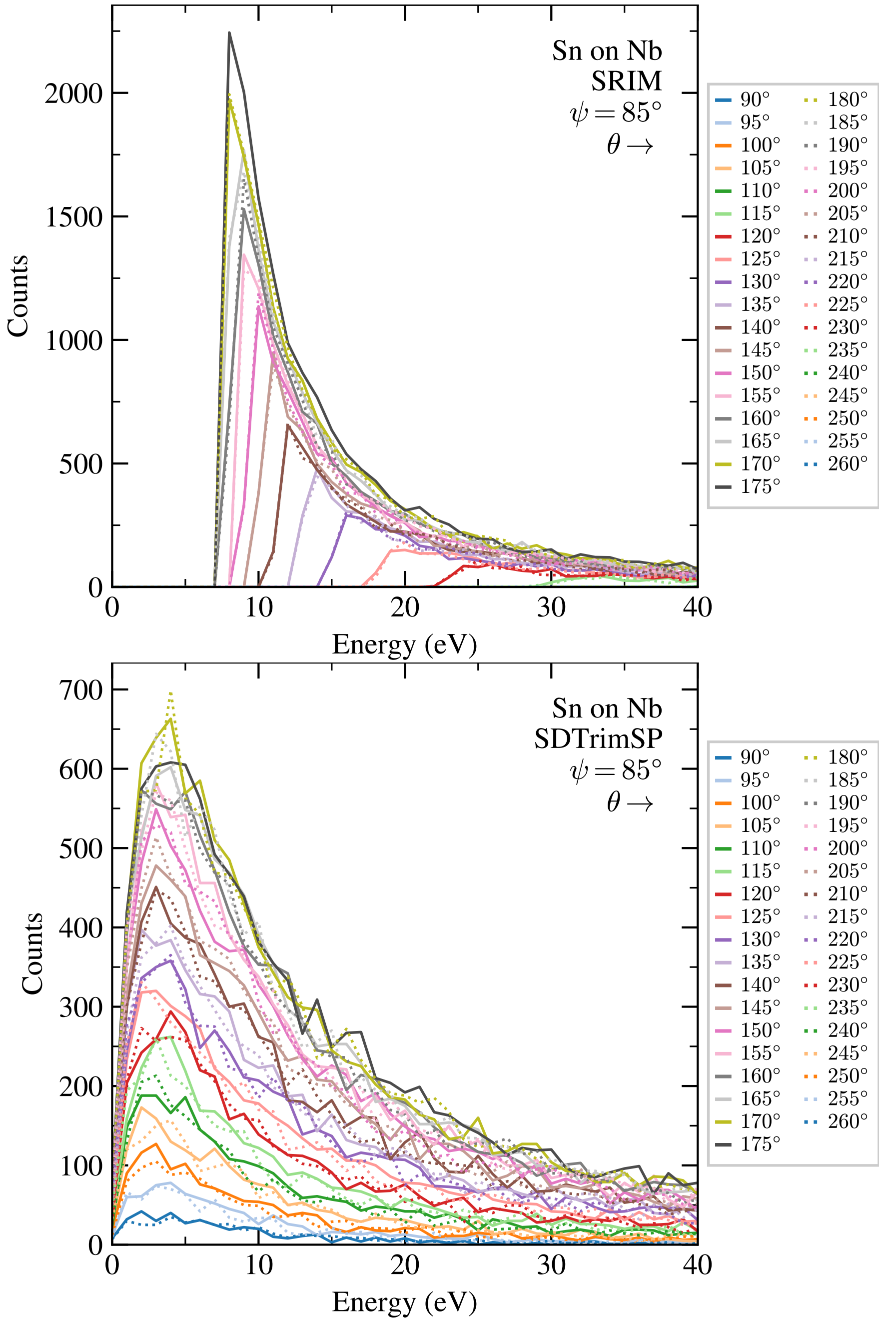

Figure A.7: Energy-count distribution plots comparing SRIM with SDTrimSP for different escape angles θ .

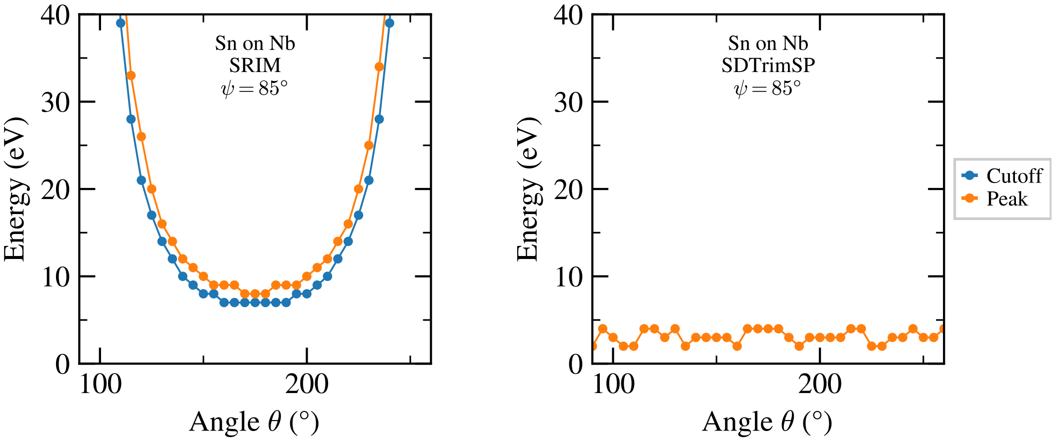

Figure A.8: Plots showing the energy peak and cutoff against the escape angle θ .

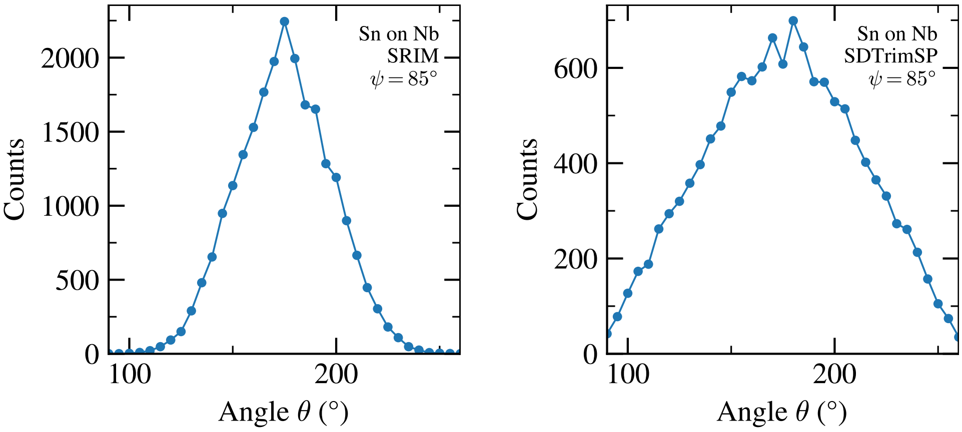

Figure A.9: Plots showing the energy peak count against the escape angle θ . The count peak in the SRIM diagram seems to be around 175° .

A.4 ▸ Mo

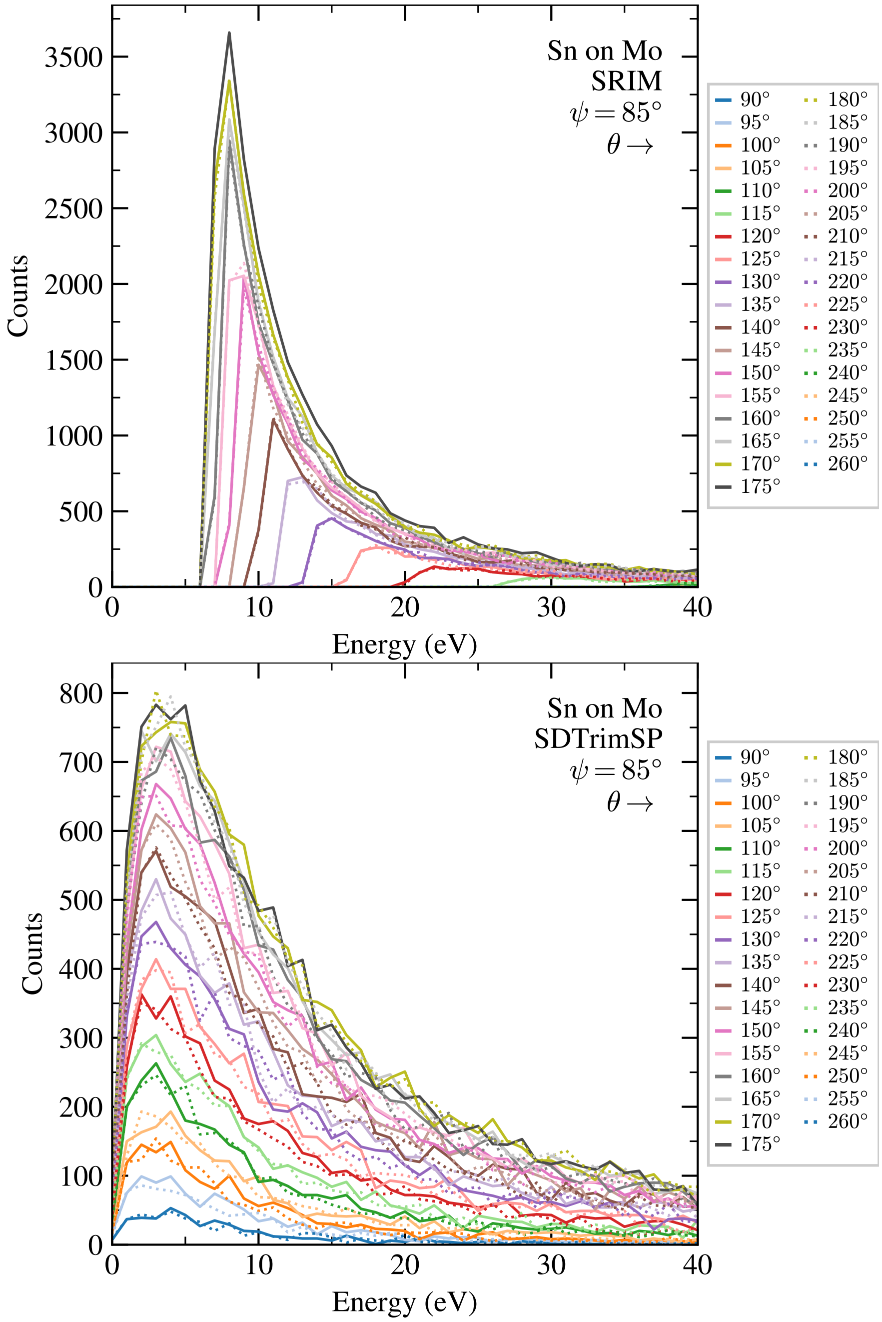

Figure A.10: Energy-count distribution plots comparing SRIM with SDTrimSP for different escape angles θ .

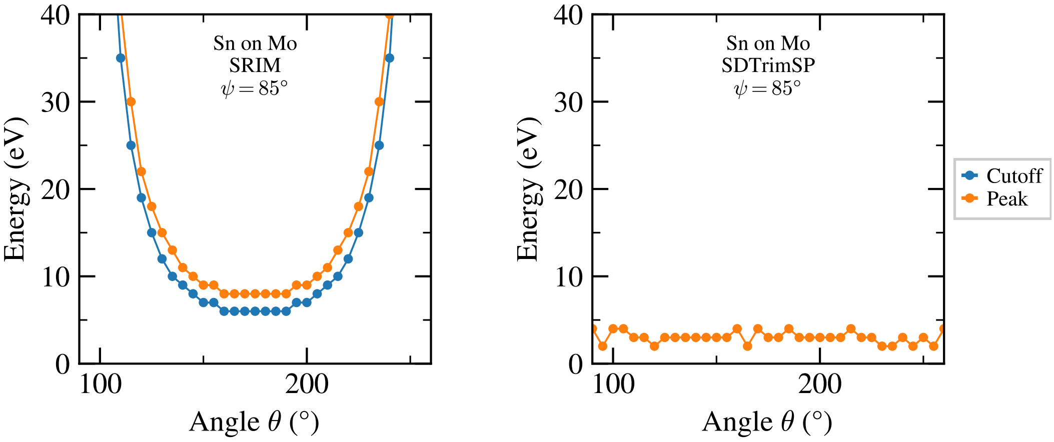

Figure A.11: Plots showing the energy peak and cutoff against the escape angle θ .

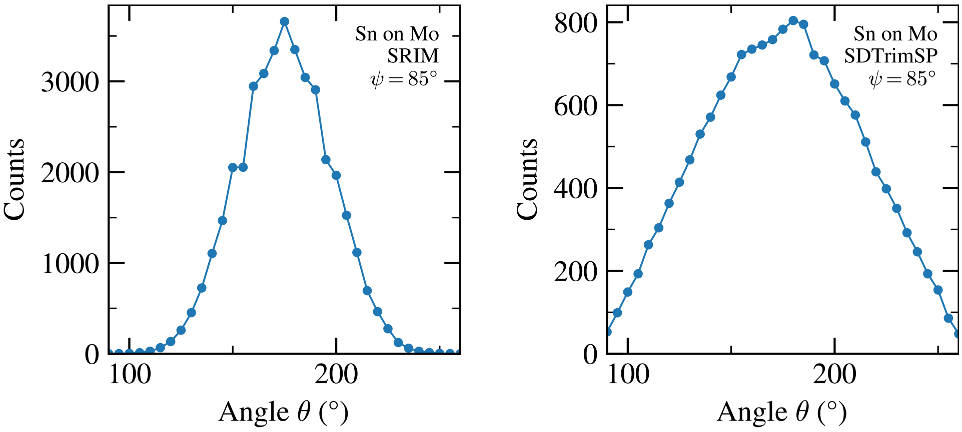

Figure A.12: Plots showing the energy peak count against the escape angle θ . The count peak in the SRIM diagram seems to be around 175° .

A.5 ▸ Tc

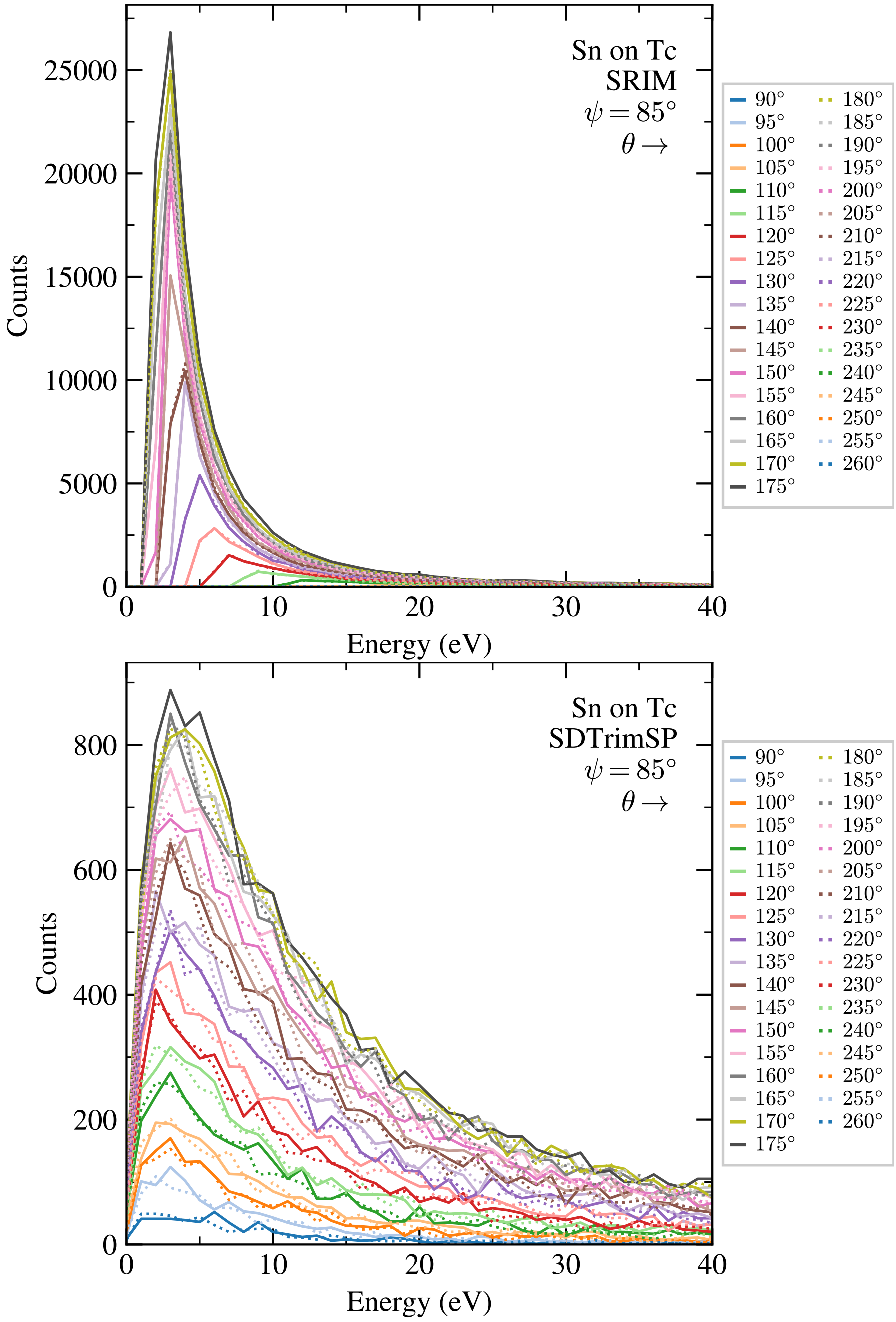

Figure A.13: Energy-count distribution plots comparing SRIM with SDTrimSP for different escape angles θ .

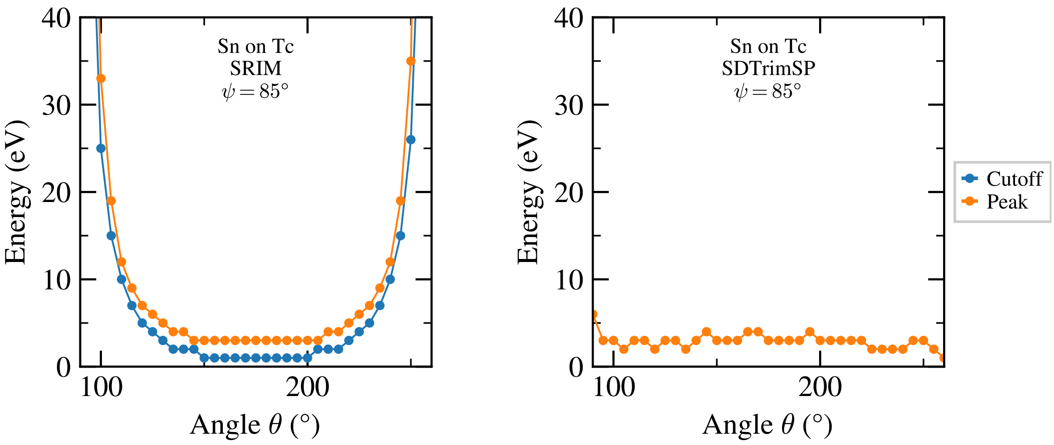

Figure A.14: Plots showing the energy peak and cutoff against the escape angle θ .

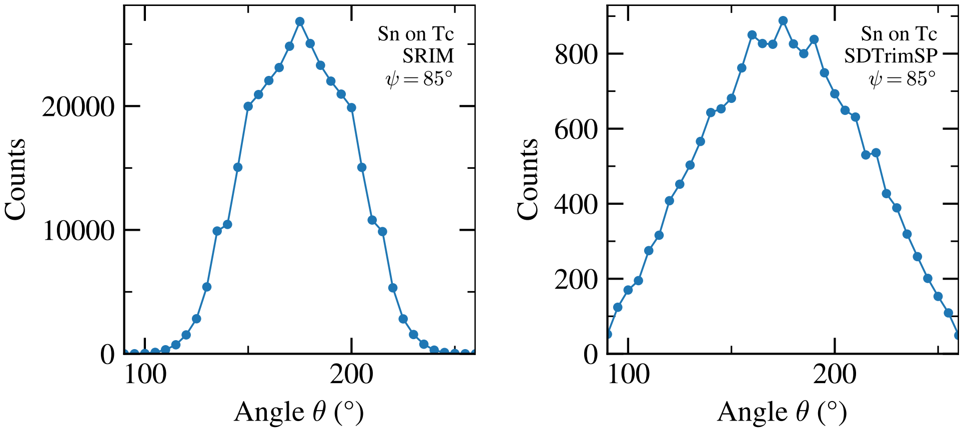

Figure A.15: Plots showing the energy peak count against the escape angle θ . The count peak in the SRIM diagram seems to be around 175° .

A.6 ▸ Ru

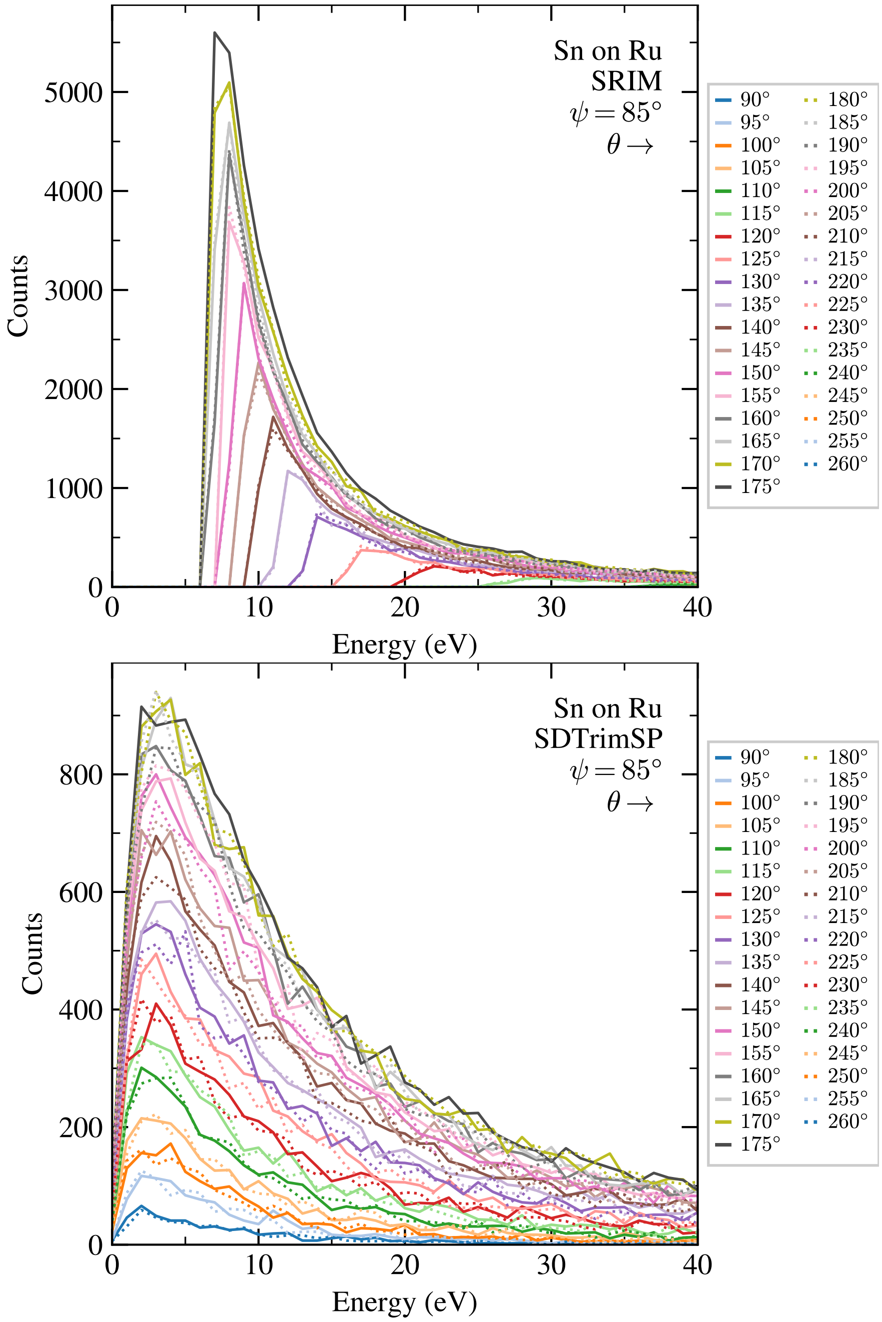

Figure A.16: Energy-count distribution plots comparing SRIM with SDTrimSP for different escape angles θ .

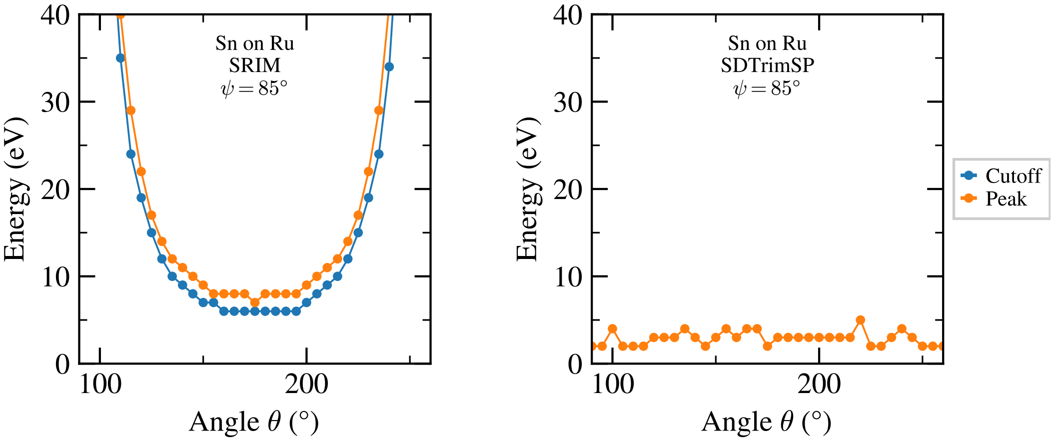

Figure A.17: Plots showing the energy peak and cutoff against the escape angle θ .

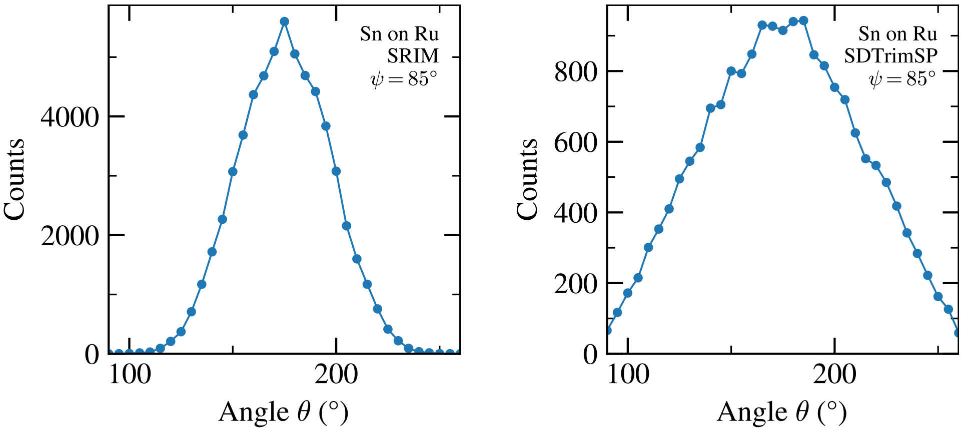

Figure A.18: Plots showing the energy peak count against the escape angle θ . The count peak in the SRIM diagram seems to be around 175° .

A.7 ▸ Rh

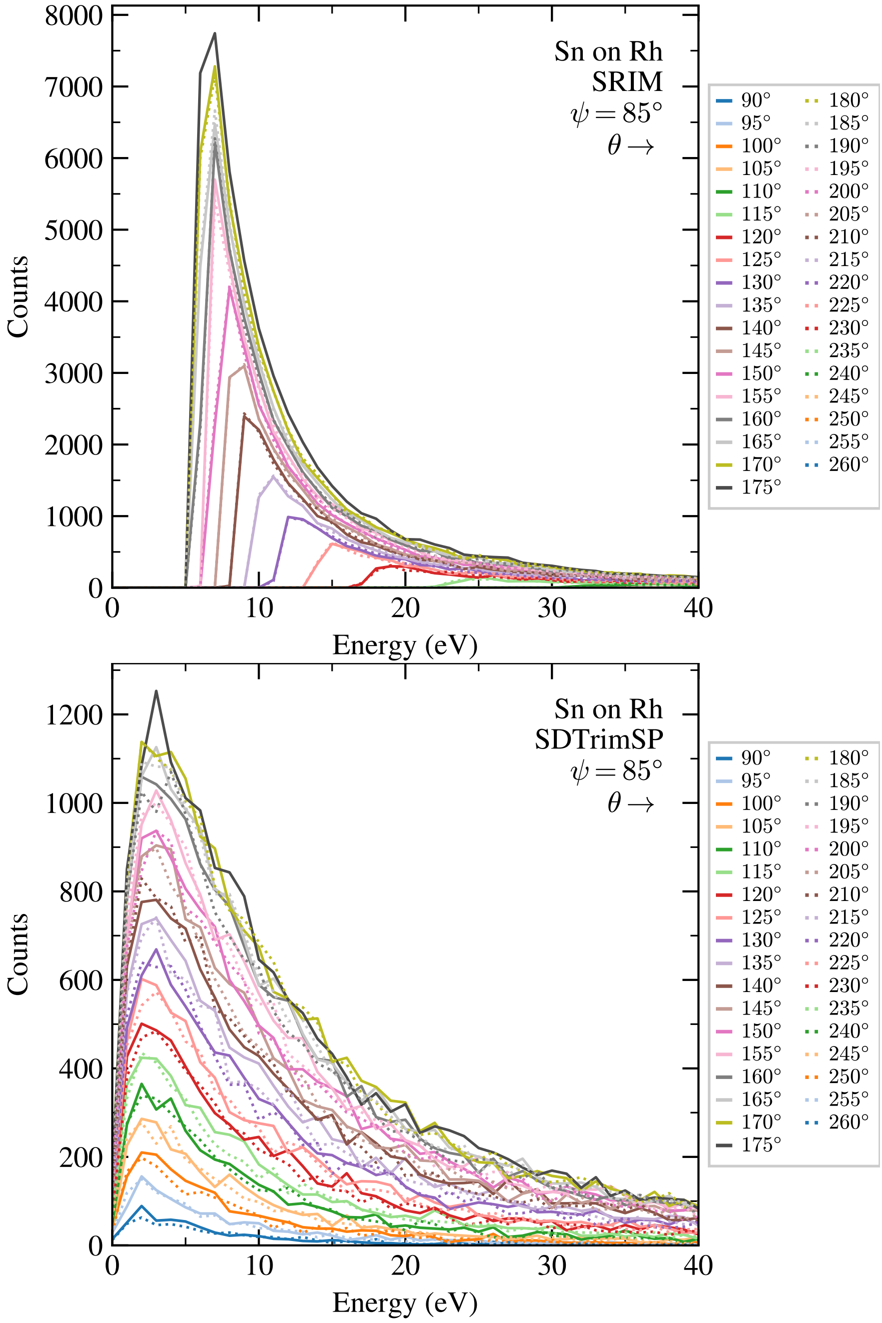

Figure A.19: Energy-count distribution plots comparing SRIM with SDTrimSP for different escape angles θ .

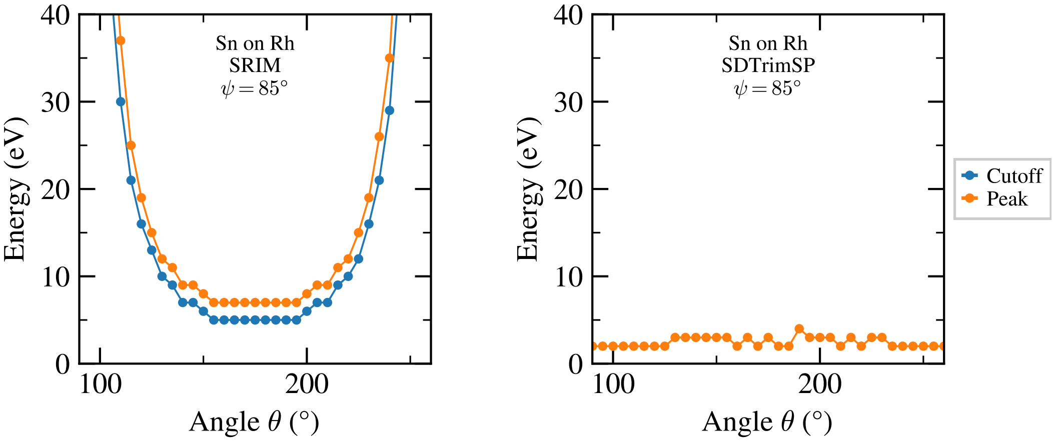

Figure A.20: Plots showing the energy peak and cutoff against the escape angle θ .

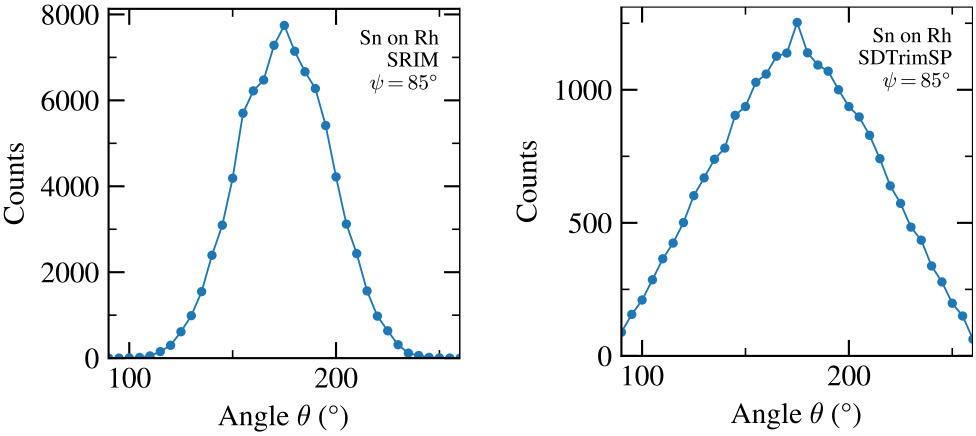

Figure A.21: Plots showing the energy peak count against the escape angle θ . The count peak in the SRIM diagram seems to be around 175° .

A.8 ▸ Pd

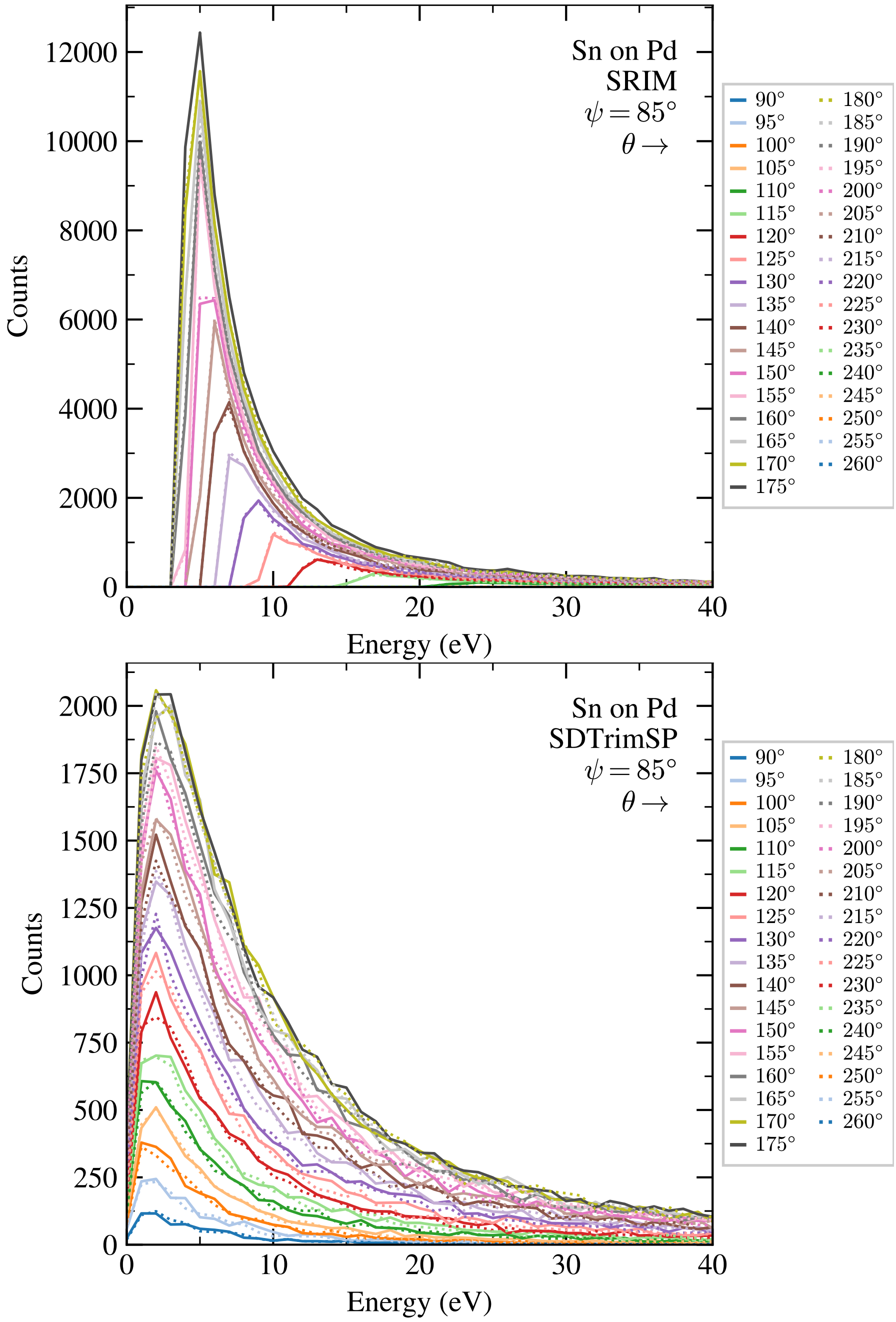

Figure A.22: Energy-count distribution plots comparing SRIM with SDTrimSP for different escape angles θ .

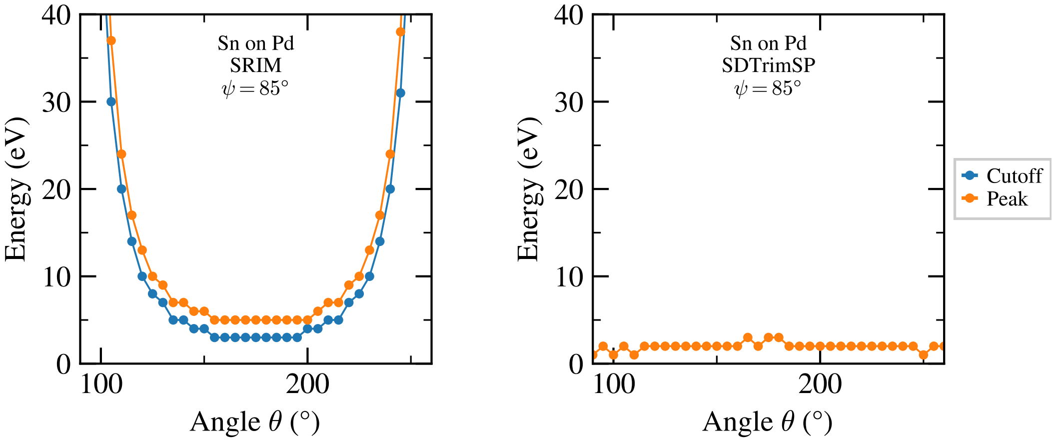

Figure A.23: Plots showing the energy peak and cutoff against the escape angle θ .

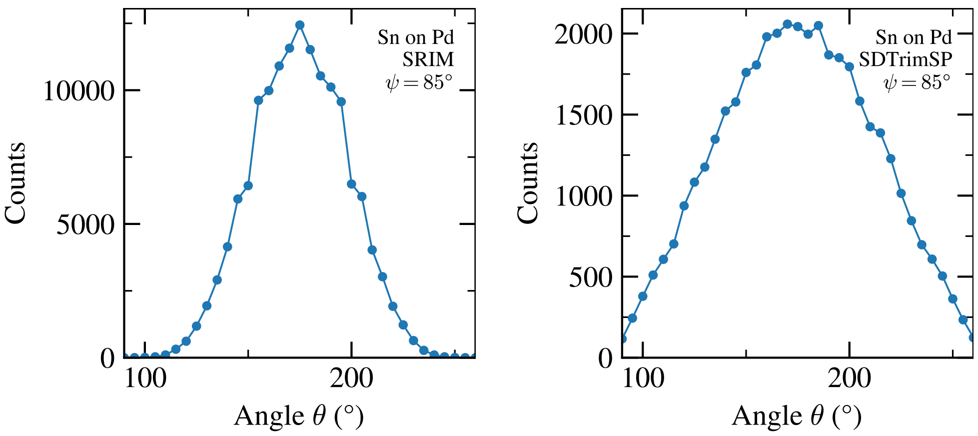

Figure A.24: Plots showing the energy peak count against the escape angle θ . The count peak in the SRIM diagram seems to be around 175° .

A.9 ▸ Ag

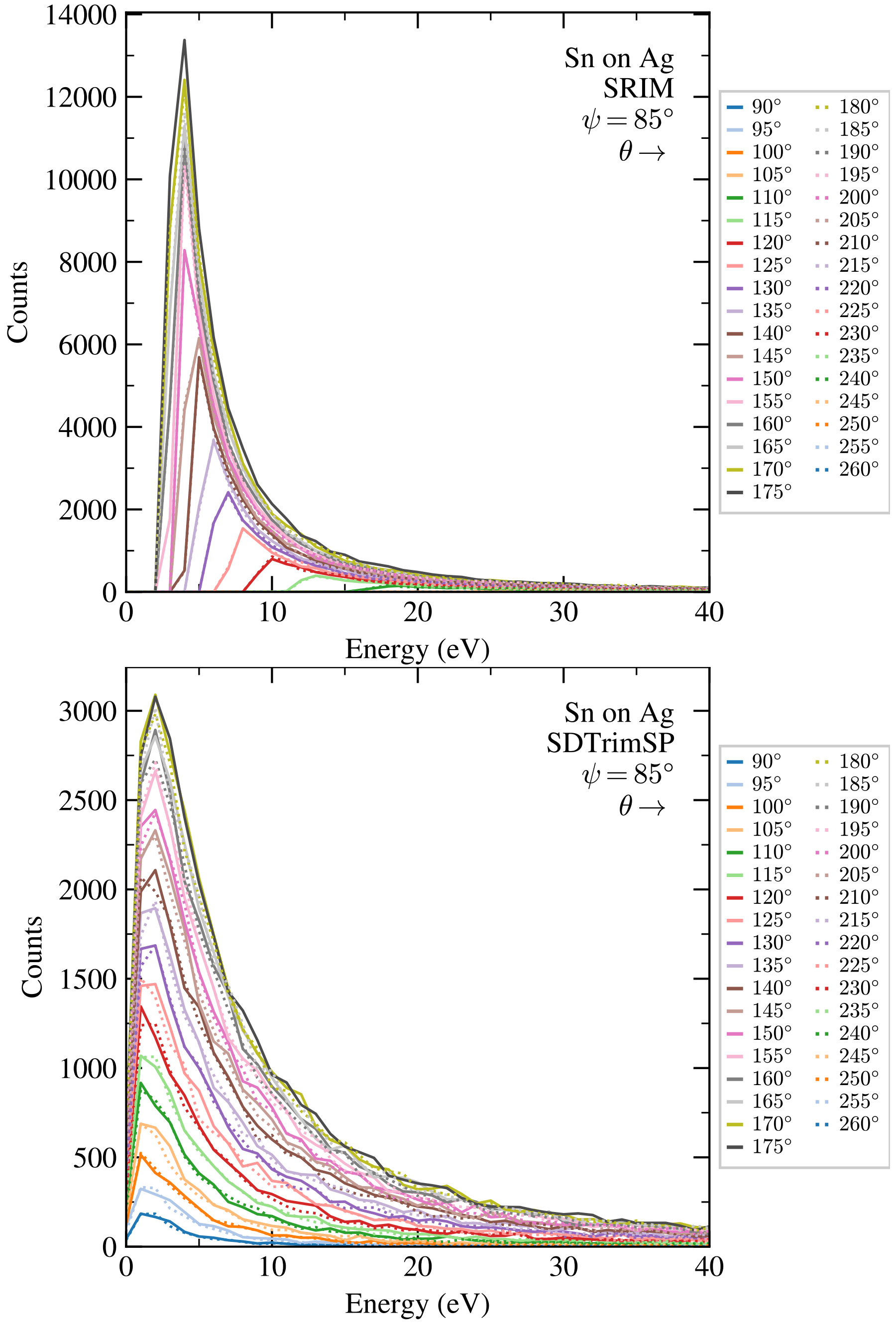

Figure A.25: Energy-count distribution plots comparing SRIM with SDTrimSP for different escape angles θ.

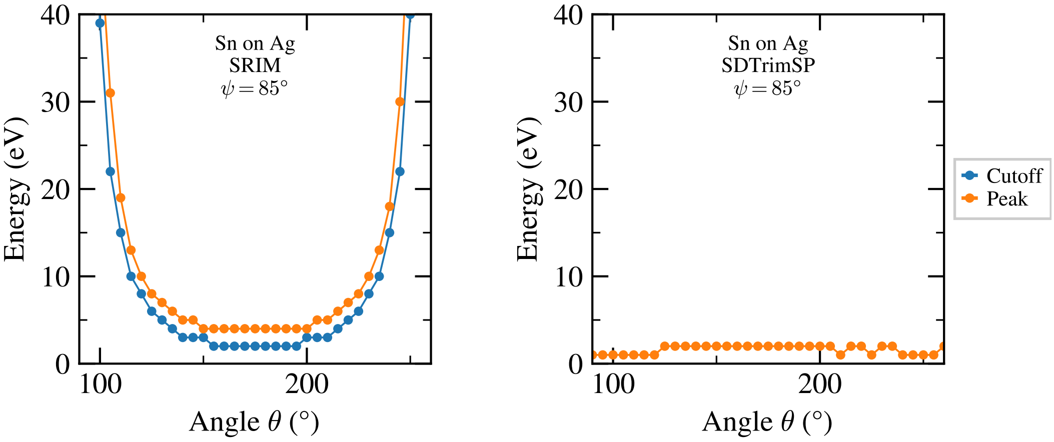

Figure A.26: Plots showing the energy peak and cutoff against the escape angle θ .

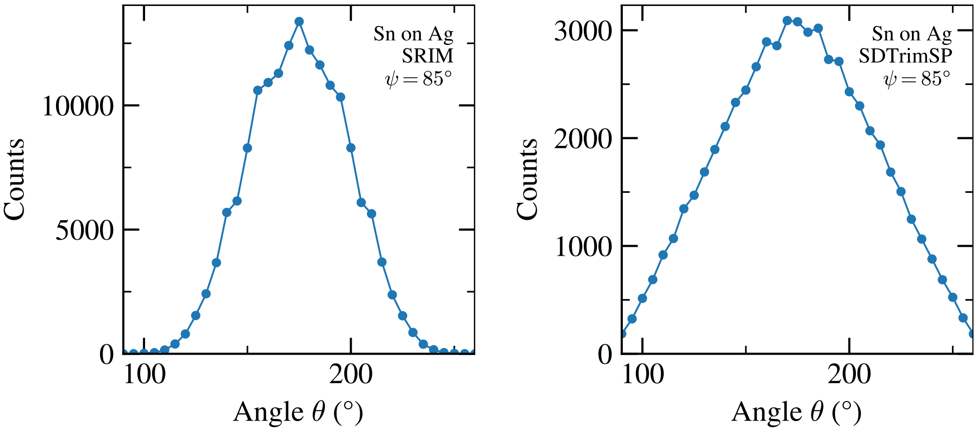

Figure A.27: Plots showing the energy peak count against the escape angle θ . The count peak in the SRIM diagram seems to be around 175° .

A.10 ▸ Cd

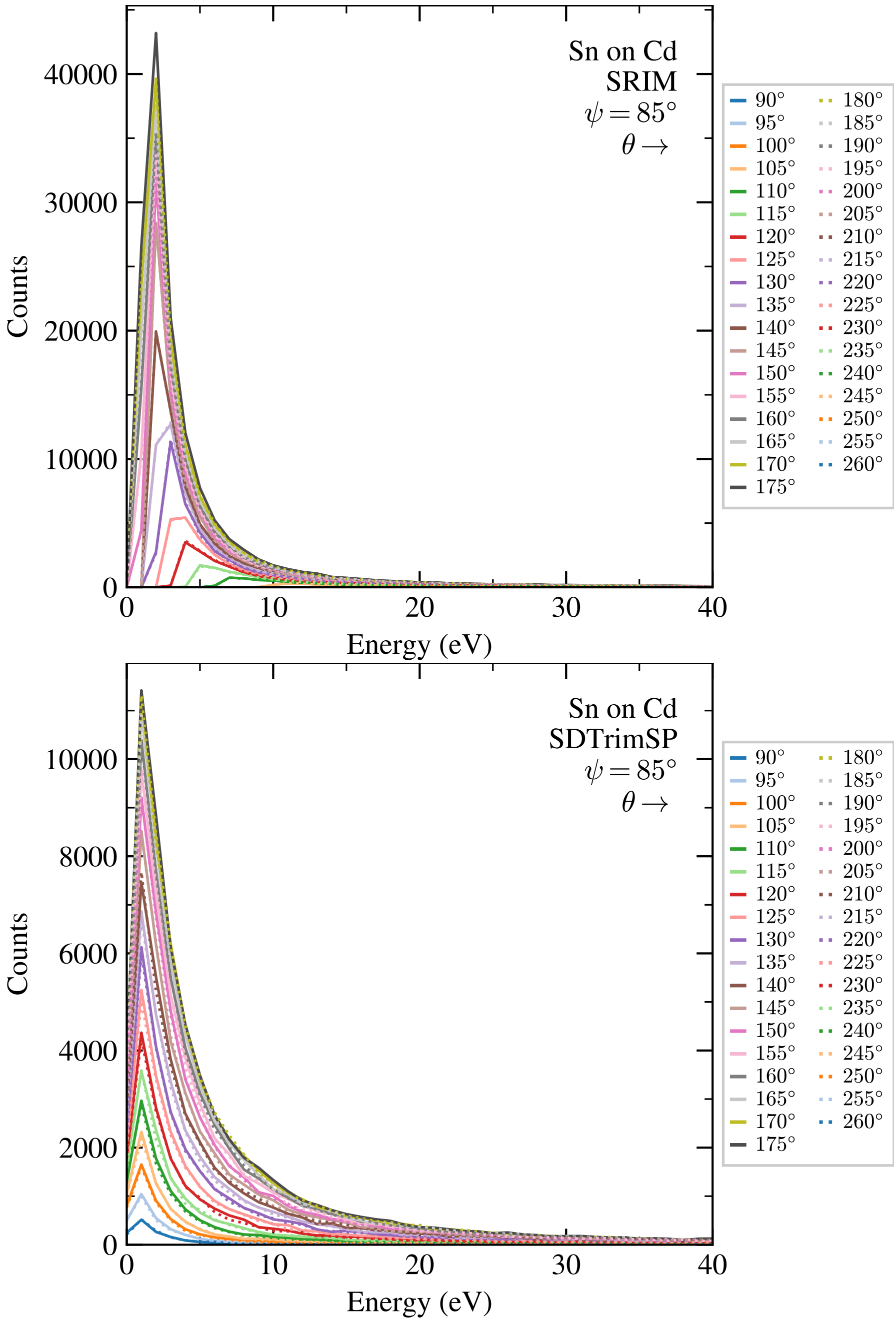

Figure A.28: Energy-count distribution plots comparing SRIM with SDTrimSP for different escape angles θ .

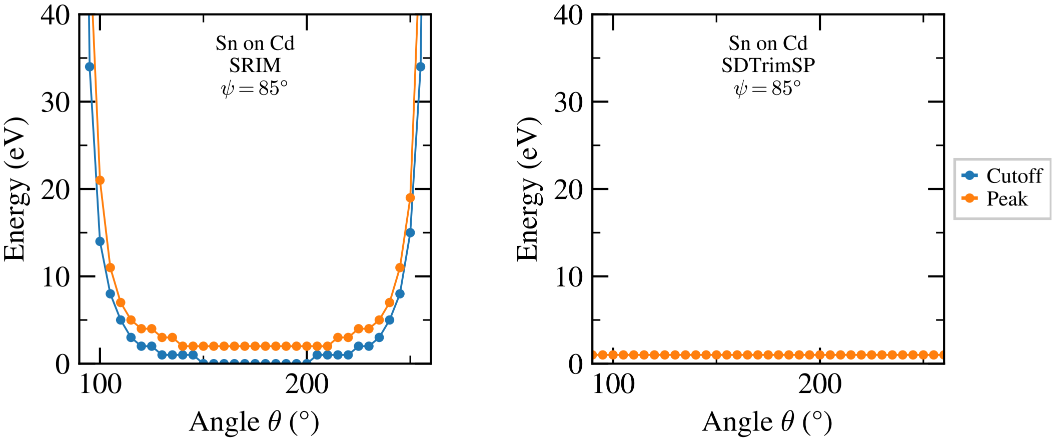

Figure A.29: Plots showing the energy peak and cutoff against the escape angle θ .

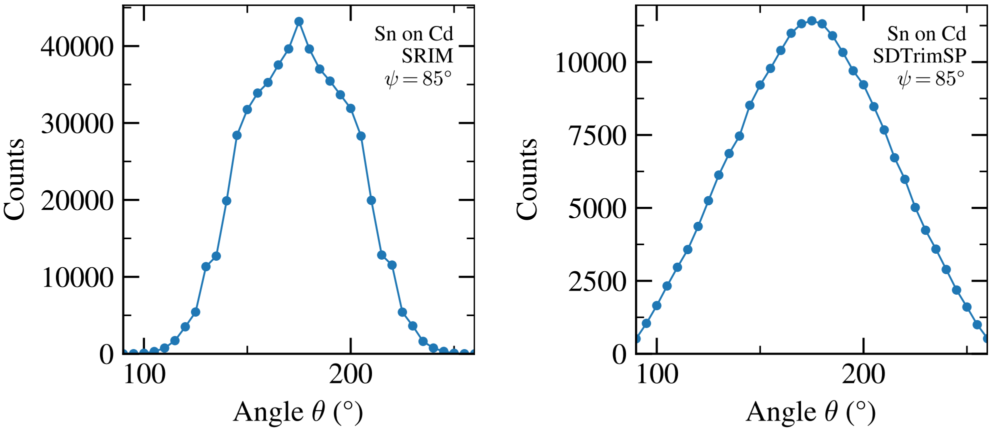

Figure A.30: Plots showing the energy peak count against the escape angle θ . The count peak in the SRIM diagram seems to be around 175° .

Bibliography

[1] F. Torretti, R. Schupp, D. Kurilovich, A. Bayerle, J. Scheers, W. Ubachs, R. Hoekstra, and O. O. Versolato, "Short-wavelength out-of-band EUV emission from sn laser-produced plasma", *Journal of Physics B: Atomic, Molecular and Optical Physics*, vol. 51, no. 4, p. 045 005, Jan. 2018. DOI: `10.1088/1361-6455/aaa593`. [Online]. Available: `https://doi.org/10.1088%2F1361-6455%2Faaa593`.

[2] M. J. Deuzeman, "Generation and interactions of energetic tin ions", English, PhD thesis, University of Groningen, 2019, ISBN: 978-94-034-1619-9.

[3] A. W. Noordam, "The scattering interaction of low energy tin ions on ruthenium", Master's thesis, University of Groningen, the Netherlands, 2019.

[4] A. Kramida, Yu. Ralchenko, J. Reader, and NIST ASD Team, *NIST atomic spectra database (ver. 5.7.1)*, National Institute of Standards and Technology, Gaithersburg, MD, 2019. DOI: `10.18434/T4W30F`. [Online]. Available: `https://physics.nist.gov/asd` (visited on Jun. 24, 2020).

[5] W. Eckstein, *Computer Simulation of Ion-Solid Interactions*. Berlin, Heidelberg: Springer Berlin Heidelberg, 1991, ISBN: 978-3-642-73513-4. DOI: `10.1007/978-3-642-73513-4`.

[6] R. Smith, Ed., *Atomic and Ion Collisions in Solids and at Surfaces: Theory, Simulation and Applications*. Cambridge University Press, 1997, ISBN: 9780511524325. DOI: `10.1017/CBO9780511524325`.

[7] K. Oura, V. Lifshits, A. A. Saranin, A. Zotov, and M. Katayama, *Surface Science, An Introduction*. Berlin, Heidelberg: Springer Berlin Heidelberg, 2003, ISBN: 978-3-662-05179-5. DOI: `10.1007/978-3-662-05179-5`.

[8] J. R. Taylor, *Classical Mechanics*. US: University Science Books, 2004, ISBN: 978-1-891389-22-1.

[9] Caiciss.co.uk, *Kinematic factor derivation*. [Online]. Available: `http://www.caiciss.co.uk/kinematic.pdf` (visited on Jun. 16, 2020).

[10] R. D. Levine, *Molecular Reaction Dynamics*. Cambridge University Press, 2009, ISBN: 978-0521140713.

[11] A. Anders, "Tutorial: Reactive high power impulse magnetron sputtering (r-HiPIMS)", *Journal of Applied Physics*, vol. 121, no. 17, p. 171 101, Mar. 2017. DOI: `10.1063/1.4978350`. [Online]. Available: `https://doi.org/10.1063/1.4978350` (visited on Jun. 20, 2020).

[12] J. F. Ziegler, *Srim; the stopping and range of ions in matter*. [Online]. Available: `http://www.srim.org/SRIM/SRIMINTRO.htm` (visited on Jun. 22, 2020).

[13] J. F. Ziegler, J. Biersack, and M. D. Ziegler, "Trim–setup and input", in *SRIM - the stopping and range of ions in matter*. Chester, Maryland : SRIM, 2008, ch. 8, ISBN: 978-0-9654207-1-6. [Online]. Available: `http://www.srim.org/SRIM/SRIM%2008.pdf` (visited on Jun. 22, 2020).

[14] H.-P. Deutsch and M. W. Beinker, "Monte carlo simulations", in *Derivatives and Internal Models: Modern Risk Management*. Cham: Springer International Publishing, 2019, pp. 207–225, ISBN: 978-3-030-22899-6. DOI: `10.1007/978-3-030-22899-6_11`. [Online]. Available: `https://doi.org/10.1007/978-3-030-22899-6_11` (visited on Jun. 22, 2020).

[15] M. Montazerian and E. D. Zanotto, "The glassy state", in *Reference Module in Materials Science and Materials Engineering*, Elsevier, 2019, ISBN: 978-0-12-803581-8. DOI: `https://doi.org/10.1016/B978-0-12-803581-8.11728-X`. [Online]. Available: `http://www.sciencedirect.com/science/article/pii/B978012803581811728X` (visited on Jun. 22, 2020).

[16] H. Hofsäss, K. Zhang, and A. Mutzke, "Simulation of ion beam sputtering with sdtrimsp, tridyn and srim", *Applied Surface Science*, vol. 310, pp. 134–141, 2014, Selected manuscripts arising from the 18th International Conference on Surface Modification of Materials by Ion Beams (SMMIB-2013), ISSN: 0169-4332. DOI: `https://doi.org/10.1016/j.apsusc.2014.03.152`. [Online]. Available: `http://www.sciencedirect.com/science/article/pii/S016943321400703X` (visited on Jun. 20, 2020).

[17] K. Sugiyama, K. Schmid, and W. Jacob, "Sputtering of iron, chromium and tungsten by energetic deuterium ion bombardment", *Nuclear Materials and Energy*, vol. 8, pp. 1–7, 2016, ISSN: 2352-1791. DOI: `https://doi.org/10.1016/j.nme.2016.05.016`. [Online]. Available: `http://www.sciencedirect.com/science/article/pii/S2352179116300126` (visited on Jun. 24, 2020).

[18] J. F. Ziegler, J. P. Biersack, and M. D. Ziegler, *SRIM - the stopping and range of ions in matter*, version SRIM-2013.00. [Online]. Available: `http://www.srim.org/SRIM/SRIMLEGL.htm` (visited on Jul. 24, 2020).

[19] J. F. Ziegler, J. Biersack, and M. D. Ziegler, “Trim: Output files”, in *SRIM - the stopping and range of ions in matter*. Chester, Maryland : SRIM, 2008, ch. 9, ISBN: 978-0-9654207-1-6. [Online]. Available: `http://www.srim.org/SRIM/SRIM%2009.pdf` (visited on Jun. 11, 2020).

[20] *Informations for program sdtrimsp*. [Online]. Available: `http://www2.ipp.mpg.de/~stel/SDTrimSP.html` (visited on Jun. 23, 2020).

[21] A. Mutzke, R. Schneider, W. Eckstein, R. Dohmen, K. Schmid, U. von Toussaint, and G. Badelow, *Sdtrimsp version 6.00*, Max-Planck-Institut für Plasmaphysik, 2019. [Online]. Available: `https://pure.mpg.de/rest/items/item_3026474_2/component/file_3026477/content` (visited on Jun. 24, 2020).

[22] A. Mutzke, R. Schneider, and G. Bandelow, “Sdtrimsp-2d: Simulation of particles bombarding on a two dimensional target - version 2.0”, 2009. [Online]. Available: `https://www.semanticscholar.org/paper/SDTrimSP-2D%3A-Simulation-of-Particles-Bombarding-on-Mutzke-Schneider/8fc6ada62bb5f8ce0c3ac9829d17d91ae106f8fa` (visited on Jun. 24, 2020).

[23] J. Coursey, D. Schwab, J. Tsai, and R. Dragoset, *Atomic weights and isotopic compositions (version 4.1)*, National Institute of Standards and Technology, Gaithersburg, MD, 2015. [Online]. Available: `http://physics.nist.gov/Comp` (visited on Jun. 24, 2020).

[24] J. Rumble, *CRC handbook of chemistry and physics*, CRC Press, 2019. [Online]. Available: `http://hbcponline.com` (visited on Jun. 24, 2020).

Index